Derivation of a Qualitative Model for the Spatial Characteristic Wavelength of Extrusion Flow Instabilities: Investigation of a Polybutadiene Rubber through Capillary, Slit and Complex Geometry Extrusion Dies

Christos K. Georgantopoulos, Masood K. Esfahani, Michael A. Pollard, Ingo F. C. Naue, Andrea Causa, Roland Kádár, and Manfred Wilhelm*

The extrusion flow instabilities of commercial polybutadiene (PBD) are investigated as a function of the different extrusion die geometries, such as round capillary, slit, and complex cross-section profile slit dies via capillary rheology. Qualitative models are used to fit the experimental data for the spatial characteristic wavelength (λ) of the appearing extrusion flow instabilities. A new qualitative model for the slit die geometry, rectangular cross-section, is derived based on the theoretical concept of the "two layers" extrudate and the force balance at the die exit region. The proposed qualitative model for the slit die geometry is used to predict the spatial characteristic wavelength (λ) for extrudates obtained by complex cross-section profile slit die geometries similar to industrial manufacturing. Correlation between the ratio of the extensional (Y_s) and shear (σ_x) stress at the die exit area and the characteristic dimension, height H for slit dies and diameter D for round capillary dies, is presented. Moreover, a geometry-dependent model is used to predict the spatial characteristic wavelength (λ) of the extrusion flow instabilities from a round capillary die to a slit die and vice versa.

C. K. Georgantopoulos, M. K. Esfahani, M. A. Pollard, I. F. C. Naue, M. Wilhelm
Karlsruhe Institute of Technology (KIT)
Institute of Chemical Technology and Polymer Chemistry (ITCP)
Engesserstraße 18, 76131 Karlsruhe, Germany
E-mail: manfred.wilhelm@kit.edu
A. Causa
Pirelli Tyre S. p. A.
R&D
Viale Piero e Alberto Pirelli 25
Milan 20126, Italy
R. Kádár
Chalmers University of Technology
Department of Industrial and Materials Science
Division of Engineering Materials
Gothenburg SE-412 96, Sweden

1. Introduction

Extrusion flow instabilities during polymer melt processing have been one of the most commonly encountered problems in the polymer-related industry over the last 60 years. Typically, extrusion flow instabilities are categorized by the type of surface and/or volume distortions named as sharkskin, stick-slip, and gross melt fracture (GMF).[1–10]

The molecular mechanism behind the macroscopic extrusion flow instabilities is still under investigation. For the origin of sharkskin instability, possible scenarios include the extensional (Y_s) stress at the die exit region, or in the fluctuation of a polymer chain between coiled-stretched and entangled-disentangled states on the lip of the die exit.[6,7] The origin of stick-slip is based on a sudden disentanglement-entanglement procedure between polymer chains adsorbed on the die wall and the bulk polymer chains.[3,4,6,7] The origin of gross melt fracture (GMF) is based on the turbulent flow at the die entrance region.[6,7] These concepts have not been clarified and proven yet, although a plethora of studies is in agreement that the sharkskin and any surface distortions probably originate at the die exit region.[4,8,11]

Supporting the concept that the sharkskin/melt fracture surface distortions originate at the die exit region, Cogswell[12] presented a theoretical approach that focuses on the extensional (Y_s) stress directly outside of the die exit. Cogswell[12] assumed first that the polymer on the boundary condition, that is on the wall of the die lip area just before exiting it, has almost zero velocity. Second, directly after the die exit, the swelling phenomenon happens and extensional (Y_s) stress is developed surrounding the exit of the die lip. Hence, the extensional (Y_s) stress on the surface of the extrudate is becoming non-linear, and a tear-like behavior starts due to the time dependency at the exit. The tear creates a flow discontinuity and splits the material into two distinct layers: the theoretical macroscopic layer near the wall, called the surface layer, which develops the instability distortion; and the core layer, which becomes the "valley" like formation. The concept proposed by Cogswell[12] for the "two layers" extrudate model

**ADVANCED
SCIENCE NEWS**

www.advancedsciencenews.com

[M]acro-
molecular

Materials and Engineering

www.mame-journal.de

has been experimentally observed by El Kissi et al.,[13–15] and Piau et al.[16] for polydimethylsiloxane (PDMS), Inn et al.[17] and Piau et al.[18] for polybutadiene (PBD), Migler et al.[19] for linear low-density polyethylene (LLDPE) and Georgantopoulos et al.[20–22] for styrene-butadiene rubbers (SBR).

Burghelea et al.[23,24] investigated linear low density polyethylene (LLDPE, M_w = 148 kg mol^{-1}, Đ = 4.2) and low density polyethylene samples (LDPE, M_w = 256 kg mol^{-1}, Đ = 15) using a laser-doppler velocimetry (LDV) technique. They proposed[23,24] that at the die exit region the velocity distribution and the extensional (Y_s) stress on the surface layer of the extrudate are responsible for the onset of surface fracture, related to the sharkskin instability. Specifically, they suggested that on the surface of the extrudate around the die periphery the material experiences an intensive extensional flow. Primary computational simulations coupled with experimental work by Tremblay,[25] Rutgers, and Mackley[26] evaluate that the extrusion surface distortions correlate with the extensional (Y_s) stress on the surface layer of the extrudate at the die exit region. Shortly after the extrudate leaves the die exit the extensional (Y_s) stress has a higher magnitude on its surface layer and decreases into the core layer, where the shear (σ_x) stress is dominant.[19,25,26] Specifically, as the extrusion throughput is increased, a larger surface area is vulnerable to tear behavior, and for this reason, the phenomenon becomes more intensive as the throughput increases.[19] Computational simulations using the finite element method by Venet and Verges[27] provide evidence of tangential stress located on the surface of the extrudate surrounding the perimeter of the round capillary die exit. The magnitude of the tangential stress increases as the flow rate increases. Advanced numerical studies by Karapetsas et al.,[28] Pettas et al.,[29] and Varchanis et al.[30] proposed that the onset of sharkskin instability originates at the die exit region where a combination of an intensive extensional deformation at the die exit and the recoil relaxation effect of the polymeric chain is observed.

Wang and coworkers,[31–33] and Inn et al.[17] developed simple analytical models which describe the development of the spatial characteristic wavelength λ of extrudates through round capillary dies as a function of extrudate velocity. Wang and coworkers[31–33] studied linear low-density polyethylene (LLDPE, M_w = 112 kg mol^{-1}, Đ = 4.15) and defined the spatial characteristic wavelength as $λ = \langle V \rangle \tau^*$, where $\langle V \rangle$ is the average extrudate velocity and τ^* is the characteristic time periodicity of the phenomenon. Inn et al.[17] studied a specific polybutadiene sample (PBD, M_w = 182 kg mol^{-1}, Đ = 1.90) and describe the development of the spatial characteristic wavelength λ based on the force balance at the die exit region using the Cogswell[12] "two-layer" model for the extrudate. Georgantopoulos et al.[22] used the Inn et al.[17] model to fit experimental data of the spatial characteristic wavelength λ obtained by round capillary dies for several SBR samples. Georgantopoulos et al.,[22] based on the previously reported experimental and numerical studies[23–30] assumed that the extensional (Y_s) stress on the surface layer of the extrudate at the die exit region has a larger magnitude than the theoretical shear (σ_x) stress on the interface between the two layers (surface and core), $Y_s > \sigma_x$. The authors[22] presented correlations between the stress ratio (Y_s/σ_x) at the die exit region and molecular properties such as the longest relaxation time, τ_d and molecular architecture (linear, branched) of the investigated samples. These correlations are in agreement with the assumptions of Wang and coworkers,[31–33] Inn et al.[17] and Rutgers and Mackley[26] that the ratio of the stress (Y_s/σ_x) at the die exit region has a dependency on the molecular weight and architecture of the extruded polymers. Moreover, the obtained values of the stress ratio at the die exit region, are larger than one, $Y_s/\sigma_x > 1$; consequently, their initial assumption is confirmed.[22]

Within this study, the extrusion flow instabilities of commercial polybutadiene (PBD) samples are investigated as a function of die geometries. The models of Wang and coworkers,[31–33] and Inn et al.[17] are presented. A new model for slit dies (rectangular cross-section area) based on the Inn et al.[17] methodology, Cogswell's[12] "two-layers" extrudate model, and Ovaici et al.[34] concept for the force balance at the die exit region is derived. The proposed qualitative model for the slit die geometry is used to predict the spatial characteristic wavelength λ for extrudates obtained by traditional slit dies with different dimensions and two complex cross-section profile slit die geometries similar to the manufacturing process of rubber compounds in industry. In addition, a simple geometry-dependent model proposed by Georgantopoulos et al.[21] for the prediction of the spatial characteristic wavelength λ of the extrusion flow instabilities from a round capillary to a slit die and vice versa is discussed. This correlation is here tested for the investigated PBD sample and multiple round capillary and slit die geometries.

2. Material, Characterization Procedure, and Equipment

To determine the relative molecular weight distribution (MWD) of the investigated polybutadiene (PBD) sample, quadruple-detection size exclusion chromatography (SEC) was used. This quadruple-detection SEC is equipped with a differential refractive index (DRI) detector, UV detector, viscometer, and a multi-angle laser light scattering (MALLS) detector. The SEC was calibrated with homopolymer polybutadiene standards with linear molecular architecture. The MWD of the sample as obtained by the DRI detector is presented in **Figure 1**a. The responses of the quadruple-detection SEC for the elution volume distribution and the calibration curve of the polybutadiene standards are presented in Figure S1, Supporting Information. The MWD is unimodal with a weighted average molecular weight of M_w = 375 kg mol^{-1} and dispersity index Đ = M_w/M_n = 3.5, see Figure 1a and **Table 1**. In Figure 1b, the Mark–Houwink[35,36] plot is presented in order to investigate the molecular architecture (linear, branch) of the studied polybutadiene (PBD) sample. To develop the Mark–Houwink[35,36] plot, the intrinsic viscosity [η] of the sample was obtained by the viscometer detector and plotted as a function of the absolute molecular weight obtained by the MALLS detector. The obtained result is compared to polybutadiene homopolymer standards that are known to have linear molecular architecture, see Figure 1b. Between 400 to 3000 kg mol^{-1} the intrinsic viscosity of the investigated PBD deviates from the calibration standards. This deviation suggests that the molecular architecture contains branches in the range of 400 to 3000 kg mol^{-1} molecular weight.

Oscillatory shear frequency sweep experiments were performed with a rubber process analyzer (RPA) elite close cavity rheometer from TA Instruments. This rheometer is equipped
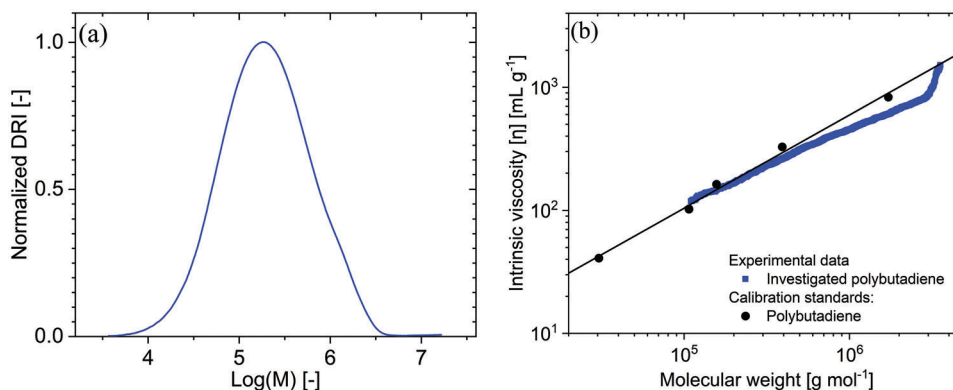
ADVANCED
SCIENCE NEWS
www.advancedsciencenews.com

[M] acro-
olecular
Materials and Engineering
www.mame-journal.de

Figure 1. a) Normalized differential refractive index (DRI) detector response as a function of the molar mass for the PBD sample as obtained by SEC. b) The intrinsic viscosity $[\eta]$ as a function of molecular weight as obtained via MALLS. The black circles are calibration standards of homopolymer polybutadiene with linear molecular architecture included in the graph. The deviation of PBD from the standard between 400 and 3000 kg mol^{-1} indicates branched molecular architecture. For the UV, viscometer, and MALLS responses see Figure S1, Supporting Information.

Table 1. Molecular weight characteristics and glass transition temperature T_g of the investigated PBD sample.

Name	M_n [kg mol^{-1}]	M_w [kg mol^{-1}]	$Đ$ [–]	$T_g^{a)}$ [°C]
PBD	107	375	3.5	−108

a) 98 wt.% cis 1,4 butadiene obtained by the material data sheet.

Figure 2. Images of the two slit die geometries with different cross-sectional profiles; a) slit-die-simple-profile and b) slit-die-scalar-profile. The computer-aided design (CAD) drawings can be found in Figure S2, Supporting Information.

with a 40 mm grooved geometry to eliminate slippage and the experiments were carried out at $T = 100$ °C between an angular frequency of $\omega = 0.06$ and 300 rad s^{-1}. The obtained magnitude of the complex viscosity, storage, and loss moduli was fitted by a five-element Maxwell model.[37] The Maxwell modes are listed in Table A1. Steady-state shear flow experiments were carried out by the ARES-G2, TA Instruments, equipped with an 8 mm grooved plate-plate geometry within $\dot{\gamma}_{app.} = 0.004$ and 0.05 s^{-1} at $T = 100$ °C as well. Non-linear transient extensional rheological experiments to characterize the molecular architecture (linear, branch) of the sample were performed by the extensional viscosity fixture (EVF) equipped with an ARES-G2 rheometer between extensional rates of $\dot{\varepsilon} = 0.01$ and 10 s^{-1} at $T = 100$ °C.

Capillary rheological experiments were carried out using a Göttfert RG 50, capillary rheometer. The sample was loaded in the capillary rheometer reservoir (30 mm reservoir diameter) and remained there for 15 min at $T = 100$ °C in order to ensure a homogenized temperature profile. In total six commercially available dies were used: three round capillary dies (circular cross-section) with length of $L = 30$ mm and diameter of $D = 1, 2,$ and 3 mm; and three slit dies (rectangular cross-section) with length of $L = 30$ mm, width of $W = 10$ mm, and height of $H = 0.5, 1,$ and 3 mm. These dies were chosen based on the systematic difference of the diameter D and height H, which influences[31–33] the spatial characteristic wavelength λ of the extrusion flow instabilities. In addition to the commercial die geometries, two Equation (2) slit die geometries with different profiles of the cross-sectional area are also investigated. Automotive-related manufacturers use slit dies with complex cross-sectional profiles which enable the extrudates to have a specific shape.[38] Within this study two slit dies with differing cross-section profiles are used. The first one
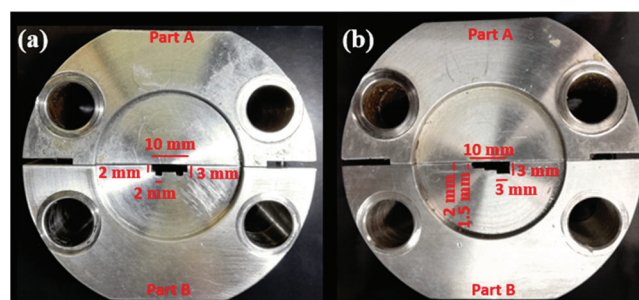
is called slit-die-simple-profile and has a length of $L = 30$ mm, a width of $W = 10$ mm, and height of $H = 2$ and 3 mm, see **Figure 2**a. The second one is called slit-die-scalar-profile and has length of $L = 30$ mm, width of $W = 10$ mm, height of $H = 1.5, 2,$ and 3 mm, see Figure 2b. The computer-aided design (CAD) drawings can be found in Figure S2, Supporting Information. Both slit dies with the cross-section profile are inspired by the review study of J. F. T. Pittman.[38]

3. Modeling Section and Rheological Models

Rheological models discussed below have been used to fit the magnitude of the complex viscosity $|\eta(\omega)|$ and the steady state viscosity $\eta(\dot{\gamma}_{app.})$ as a function of angular frequency ω and apparent shear rate $\dot{\gamma}_{app.}$, respectively. The Inn et al.[17] model for the spatial characteristic wavelength $\lambda^{Capillary}$ of the extrudates obtained by round capillary dies and the newly derived model of the spatial characteristic wavelength λ^{Slit} of the extrudates obtained by slit dies are presented. In addition, simplifications based on experimental results are used to make the Inn et al.,[17] and the new proposed model easier to handle. Finally, the proposed model by Georgantopoulos et al.[21] for the prediction of the spatial characteristic wavelength λ from round capillary to slit dies and vice versa is discussed.

**ADVANCED
SCIENCE NEWS**
www.advancedsciencenews.com

[M] acro-
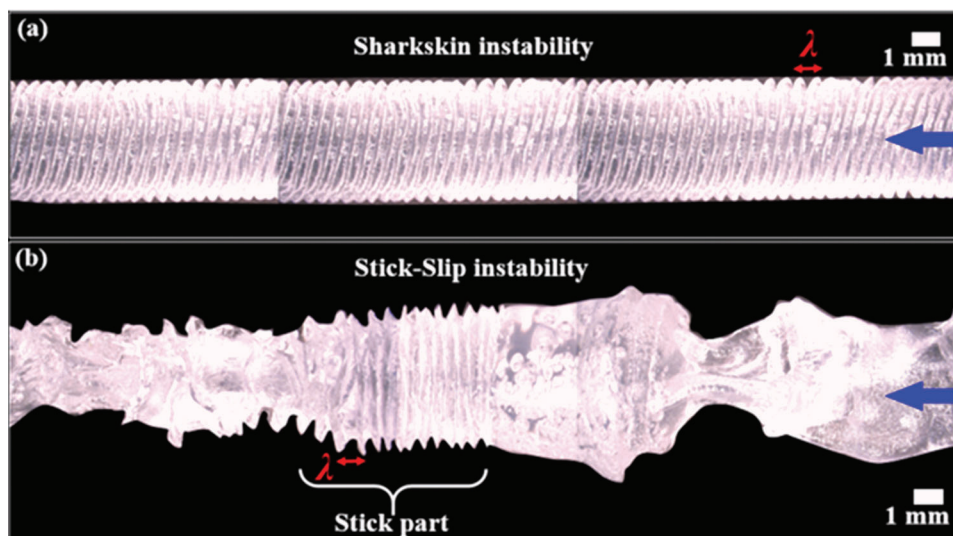molecular
Materials and Engineering
www.mame-journal.de

Figure 3. Images of extrusion flow instabilities of the investigated PBD, a) sharkskin at $\dot{\gamma}_{app.} = 10$ s^{-1} and b) stick-slip at $\dot{\gamma}_{app.} = 20$ s^{-1}. The spatial characteristic wavelength λ is indicated on the images. The extrudates were obtained by a round capillary die with $L = 30$ mm and $D = 3$ mm at $T = 100$ °C. The optical images were obtained by incident light microscopy. The blue arrows show the flow direction.

3.1. Viscosity Models

The shear-thinning region of the magnitude complex viscosity $|\eta^*(\omega)|$ as a function of angular frequency is fitted with a power law model given by Equation (1).

$$|\eta^*(\omega)| = K\omega^{n-1} \tag{1}$$

where K and n are fitting parameters. The steady-state viscosity $\eta(\dot{\gamma}_{app.})$ as a function of apparent shear rate is fitted with the Cross model,[37] given by Equation (2).

$$\eta\left(\dot{\gamma}_{app.}\right) = \frac{\eta_0}{1 + \left(\tau\dot{\gamma}_{app.}\right)^m} \tag{2}$$

where η_0 is the zero shear viscosity, τ is the longest relaxation time, and m is the power law index. In case of $|\eta^*(\omega)| = \eta(\dot{\gamma}_{app.})$ with the numerical values of $\dot{\gamma}_{app.} = \omega$, then the empirical Cox–Merz[39] rule is applicable. Under the applicability of Cox–Merz rule the shear-thinning exponent of Equations (1) and (2) is $m = 1 - n$. As shown later the Cox–Merz rule is not applicable within the whole range of shear rates for the investigated PBD sample at $T = 100$ °C. Namely, the Cox–Merz rule is applicable within $1 s^{-1} < \dot{\gamma}_{wall} < 50 s^{-1}$, but after $\dot{\gamma}_{wall} > 50 s^{-1}$ the Cox–Merz[39] rule is not applicable.

3.2. Definitions of the Spatial Characteristic Wavelength λ

During the extrusion process of the investigated polybutadiene (PBD) sample, extrusion flow instabilities manifest themselves, see **Figure 3**. Specifically, during extrusion or within capillary rheology experiments smooth, sharkskin, stick-slip, and gross melt fracture (GMF) instabilities might occur as the shear rate increases. The spatial characteristic wavelength λ of instabilities is defined as the average distance between two consecutive similar surface distortions.[21,22] This definition can easily be applied to sharkskin extrusion flow instability, where the whole extrudate has a well-developed rather periodic pattern on its surface as Figure 3a depicts. Regarding the stick-slip instability in Figure 3b, the definition[21,22] of the spatial characteristic wavelength λ can be applied only in the stick part of the extrudate where a developed pattern similar to sharkskin exists. In the rest of the extrudate, intensive volume distortions without a specific pattern appear. Within this study, the spatial characteristic wavelength λ is defined as the one obtained by the well-developed sharkskin pattern and by the stick part of the stick-slip instability.

3.3. Derivation of a Qualitative Model for Sharkskin Applied to Round Capillary Dies

Inn et al.[17] proposed a qualitative model for the spatial characteristic wavelength λ of the extrusion flow instabilities, based on visual observation of a specific polybutadiene sample (PBD, $M_w = 182$ kg mol^{-1}, $Đ = 1.90$) extruded by round capillary dies at $T = 50$ °C. This model[17] uses the force balance[34] at the die exit to describe the formation of instability. It is assumed that the fracture instability originates at the die exit region.[17] As mentioned, this model[17] considers that the extrudate is composed of "two layers",[12] the surface layer and the core layer, see **Figure 4**. It is assumed that the two layers exist inside and outside of the die.[17]

Inn et al.[17] assumed that $R_f = X_f + h/2$. The $R_{swelled}$ is the swelled radius of the extrudate, taking into account the surface instability. Here, σ_x is the shear stress on the theoretical interface between the core and surface layer and Y_s is the extensional stress at the die exit region. The theoretical interface of those two layers is located at $r = X_0$ inside the die and at $r = X_f$ outside of the die. It is assumed[17] that immediately after the die exit, the swelling happens and the inner core layer of the extrudate swells from a radius X_0 to X_f and moves with the average extrudate velocity $V_{swelled}$. The outer surface layer is supposed to move with a different velocity, named as surface extrudate velocity $V_{extr.,surface}$.
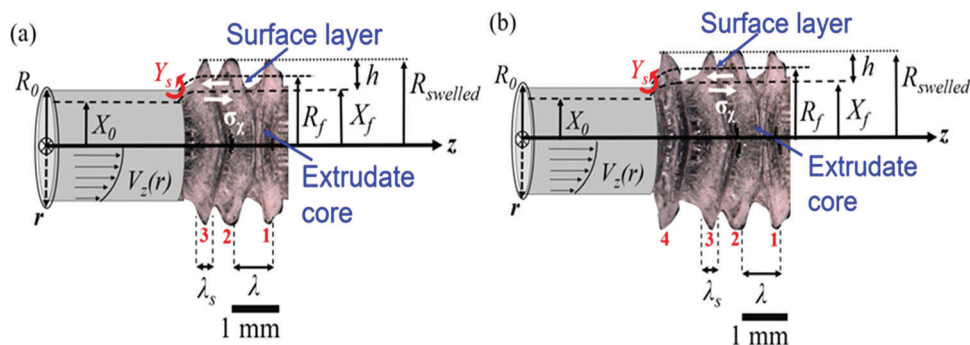
ADVANCED
SCIENCE NEWS

www.advancedsciencenews.com

[M] acro-molecular
Materials and Engineering

www.mame-journal.de

Figure 4. Schematic representation of the "two-layer" model which shows the development of flow instabilities. From a) to b) the 4th instability ridge is developed. The instability ridge, λ_s is defined as the average width (full width half maximum, fwhm) of the sharkskin stripe and it is formed by the fracture on the skin/core interface, $r = X_f$. X_0, and X_f are the theoretical radius of the core layer inside and outside of the die, respectively. R_0 and R_f are the radius of the die and the theoretical swelled radius of the extrudate if no fracture was developed, respectively. h is the spatial characteristic height of the instabilities defined as the average distance between the swelled core and the tip of the instability.

The $V_{extr.,surface}$ refers to the outer layer of the extrudate which experiences an extensional deformation immediately after the die exit region.

The derivation of this model[17] assumes a power-law fluid, and the velocity profile, see Equation (3), is given by a Poiseuille laminar flow field for a round capillary die where the slip velocity is neglected.

$$V_r(r, n) = \frac{3n+1}{n+1} \left[1 - \left(\frac{r}{R_0} \right)^{\frac{1}{n}+1} \right] \frac{Q}{\pi R_0^2} \quad (3)$$

where Q is the volumetric flow rate, R_0 is the radius of the round capillary die, and n is the power law exponent defined by $n \equiv d(log\sigma_{wall})/d(log\dot{\gamma}_{app.})$. The average velocity inside the round capillary die is given by Equation (4).

$$V_{ave.} = \frac{Q}{\pi R_0^2} \quad (4)$$

The extrudate velocity after the die swell is given by:

$$V_{swelled} = \frac{Q}{\pi R_{swelled}^2} \quad (5)$$

where $R_{swelled}$ is the radius of the swelled extrudate and D' is the swelled diameter of the extrudate, $D' = 2R_{swelled}$, see Figure 4. Combining Equations (4) and (5), Equation (6) is derived.

$$V_{ave.} = \frac{Q}{\pi R_0^2} = \frac{Q}{\pi R_{swelled}^2} \left(\frac{R_{swelled}}{R_0} \right)^2 = V_{swelled} \left(\frac{R_{swelled}}{R_0} \right)^2 \quad (6)$$

At the interface between the core and the surface layer, $V_r(r,n) = V_r(X_0,n)$, Equation (3) yields Equation (7).

$$V_r(X_0, n) = \frac{3n+1}{n+1} \left[1 - \left(\frac{X_0}{R_0} \right)^{\frac{1}{n}+1} \right] V_{ave.} \quad (7)$$

The interfacial depth parameter, ξ, is defined[17] as the ratio between the inner core radius and the theoretical radius for the surface layer if no surface fracture occurs, as follows $\xi = X_0/R_0$

$= X_f/R_f$. The interfacial depth parameter runs between $0 < \xi < 1$. The latter is explained by Equation (8), where at low shear rates $\dot{\gamma} \to 0$, the swelling effect is not pronounced and $X_f \approx R_f$, and at high shear rates $\dot{\gamma} \to \infty$, the swelling effect is obvious, so $X_f \ll R_f$.

$$\begin{aligned} \xi &= X_0/R_0 = X_f/R_f \\ \dot{\gamma} &\to 0, X_f \approx R_f, \xi \to 1 \\ \dot{\gamma} &\to \infty, X_f \ll R_f, \xi \to 0 \end{aligned} \quad (8)$$

Thus, Equation (7) coupled with Equations (6) and (8) results in:

$$\frac{V_{swelled}}{V_r(X_0, n)} = \frac{n+1}{3n+1} \left[1 - (\xi)^{\frac{1}{n}+1} \right]^{-1} \left(\frac{R_{swelled}}{R_0} \right)^{-2} \quad (9)$$

Assuming that the surface layer of the extrudate moves with $V_{extr.,surface}$, it can be calculated by:

$$V_{extr.,surface} = \frac{Q_s}{\pi R_0^2 - \pi X_0^2} = \frac{Q_s}{\pi R_0^2 (1 - \xi^2)} \quad (10)$$

where Q_s is the volumetric flow rate of the theoretical surface layer and can be obtained by Equation (11).

$$Q_s = \int_{X_0}^{R_0} (V_r 2\pi r) \, dr = \left[1 - \left(\frac{3n+1}{n+1} \right) \xi^2 + \left(\frac{2n}{n+1} \right) \xi^{3+\frac{1}{n}} \right] Q \quad (11)$$

Assuming[17] that the fracture instability forms on the surface layer of the extrudate, the ratio of the $V_{swelled}/V_{extr.,surface}$, Equation (12), is obtained by combining Equations (6), (10), and (11).

$$\frac{V_{swelled}}{V_{extr.,surface}} = \frac{1 - \xi^2}{\left(\frac{R_{swelled}}{R_0} \right)^2} \left[1 - \left(\frac{3n+1}{n+1} \right) \xi^2 + \left(\frac{2n}{n+1} \right) \xi^{3+\frac{1}{n}} \right]^{-1} \quad (12)$$

Focusing on the die exit region the force balance[34] for the round capillary die is given by Equation (13).[17]

$$2\pi X_0 \lambda_s \sigma_x = Y_s \left(\pi R_0^2 - \pi X_0^2 \right) \quad (13)$$

ADVANCED
SCIENCE NEWS
www.advancedsciencenews.com

Ｍacro-
olecular
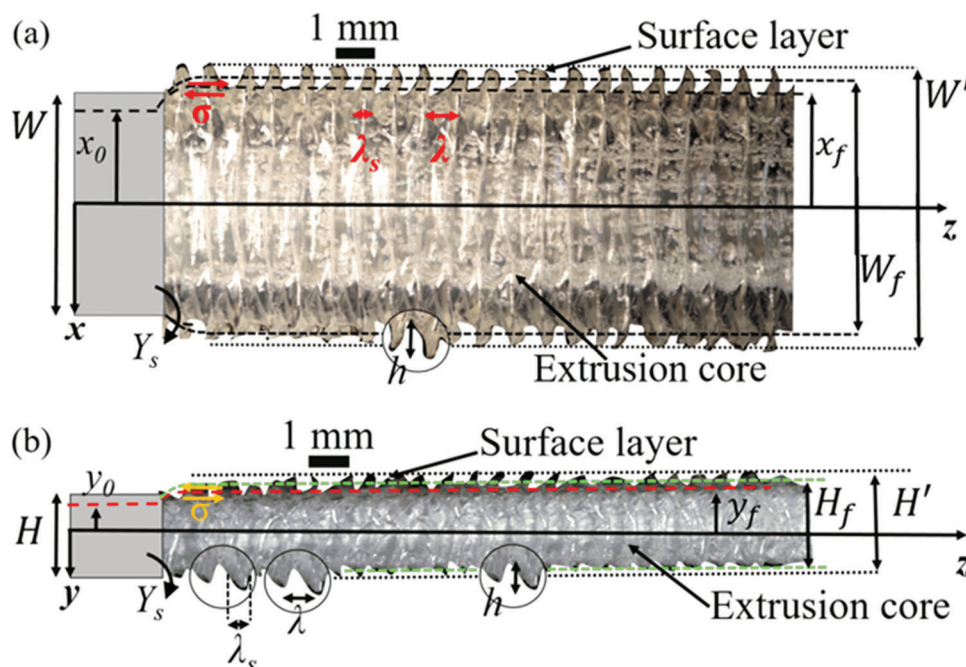Materials and Engineering
www.mame-journal.de

Figure 5. Schematic representation of the "two-layer" model for slit die geometry (rectangular cross-section area) with the width W being larger than the height H, $W > H$. a) depicts the x–z top-view and b) displays the y–z top-view of the slit die and extrudate. The instability ridge, λ_s, is defined as the average width of the sharkskin stripe, and it is formed by the fracture on the skin/core interface, see (b). x_0, y_0, x_f, and y_f are the theoretical dimensions of the core layer inside and outside of the die, respectively. The H_f and W_f are the theoretical swelled height and width of the extrudate if no fracture was developed, respectively. The parameter h is the spatial characteristic height of the instabilities defined as the average distance between the swelled core and the tip of the instability. The Inn et al.[17] assumption is used, $W_f = x_f + h/2$ and $H_f = y_f + h/2$, where H' and W' are the swelled height and width of the extrudate taking into account the surface instability. The stress σ_x is the shear stress on the theoretical interface between the core and surface layer and Y_s is the extensional stress at the die exit region.

Equation (13) presents the force balance between the shear stress σ_x on the theoretical interface between the core and surface layer, and the extensional stress Y_s at the die exit region for a capillary die with a circular cross-section area, see Figure 4. The thickness of the instability ridge λ_s is defined as the average width of the sharkskin ridge. The average distance between two consecutive similar surface distortions is defined as the spatial characteristic wavelength λ.

Inn et al.[17] assumed that the characteristic time periodicity τ^* of the instabilities is a constant ratio of $\tau^* = \lambda_s/V_{extr.,surface} = \lambda/V_{swelled}$, so $\lambda = \lambda_s(V_{swelled}/V_{extr.,surface})$. Hence, an analytical formula for the spatial characteristic wavelength λ, Equation (14), can be derived by coupling Equations (12) and (13), and $\lambda = \lambda_s(V_{swelled}/V_{extr.,surface})$.

$$\lambda = \frac{R_0}{2}\left(\frac{Y_s}{\sigma_x}\right)\left(\frac{1}{\xi} - \xi\right)\frac{1 - \xi^2}{\left(\frac{R_{swelled}}{R_0}\right)^2}\left[1 - \left(\frac{3n+1}{n+1}\right)\xi^2\right.$$

$$\left. + \left(\frac{2n}{n+1}\right)\xi^{3+\frac{1}{n}}\right]^{-1} \tag{14}$$

3.4. Derivation of a Qualitative Model for Sharkskin Applied to Slit Dies

Using the same principal ideas and assumptions of Inn et al.[17] model, a proposed qualitative model for sharkskin based on

slit die geometry is developed. This model focuses on the force balance[34] at the die exit and assumes that the fracture instability originates at the die exit region as well. Moreover, it considers that the extrudate is composed of "two layers",[12] the surface and the core layer, see **Figure 5**. It is assumed that the two layers exist inside and outside of the die as well.

The theoretical interface of those two layers is located at $x = x_0$ and $y = y_0$ inside the die and at $x = x_f$ and $y = y_f$ outside of the die. It is assumed that immediately after the die exit, the swelling happens. Hence, the inner core layer of the extrudate swells from x_0 to x_f and from y_0 to y_f. The core layer is assumed to move with $V_{swelled}$.[17] The outer surface layer is assumed to move with a different velocity called surface extrudate velocity $V_{extr.,surface}$.[17] The $V_{extr.,surface}$ refers to the outer layer of the extrudate, which experience an extensional deformation immediately after the die exit region. **Figure 6** depicts the formation of the instability ridge at the die exit region at three different time snapshots during the extrusion process at the same apparent shear rate $\dot{\gamma}_{app.} = 20 \text{ s}^{-1}$ and temperature $T = 100 \,°C$.

Assuming a power-law fluid, the velocity profile of a Poiseuille flow field for a slit die geometry, neglecting the slip velocity is described by Equation (15).[23,24]

$$V_z(y, n) = \frac{2n+1}{n+1}\left[1 - \left(\frac{2y}{H}\right)^{\frac{1}{n}+1}\right]\frac{Q}{HW} \tag{15}$$

ADVANCED
SCIENCE NEWS
www.advancedsciencenews.com

[M] acro-
molecular
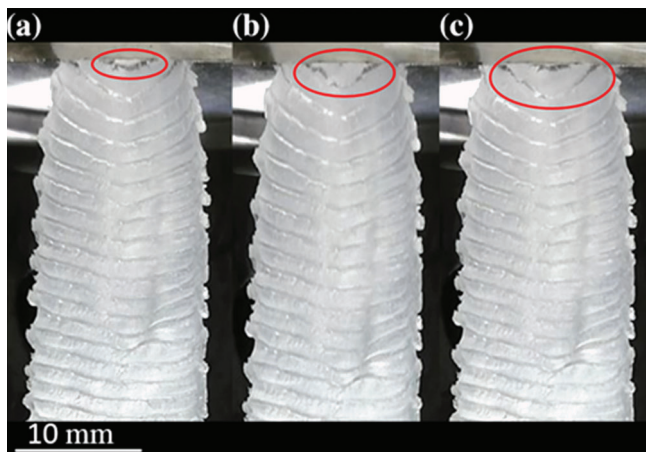Materials and Engineering
www.mame-journal.de

Figure 6. Online optical monitoring of the extrusion of the investigated PBD sample using a slit die with $L/H = 10$, $H = 3$ mm and $W = 10$ mm. The sequence of images a–c) present the same sample at three different time snapshots under steady-state conditions, a) $t = 0 + t_{exp.}$ s, b) $t = 1.5 + t_{exp.}$ S, and c) $t = 3 + t_{exp.}$ s. The development of the instability ridge is captured in the red circle and presents its evolution with the extrusion time. The extrusion conditions are $T = 100$ °C and $\dot{\gamma}_{app.} = 20$ s^{-1}.

where Q is the volumetric rate, H is the height, and W is the width of the slit die and n is the power law constant. The average velocity inside the slit die is given by Equation (16).

$$V_{ave.} = \frac{Q}{HW} \tag{16}$$

The extrudate velocity after the die swell is given by Equation (17).

$$V_{swelled} = \frac{Q}{H'W'} \tag{17}$$

Coupling Equations (16) and (17), Equation (18) derived.

$$V_{ave.} = \frac{Q}{HW} = \frac{Q}{H'W'}\left(\frac{H'W'}{HW}\right) = V_{swelled}\left(\frac{H'W'}{HW}\right) \tag{18}$$

At the interface between the core and the surface layer, $V_z(\gamma,n) = V_z(\gamma_0,n)$, Equation (15) becomes Equation (19).

$$V_z(\gamma_0, n) = \frac{2n+1}{n+1}\left[1 - \left(\frac{2\gamma_0}{H}\right)^{\frac{1}{n}+1}\right]\frac{Q}{HW} \tag{19}$$

For the slit die geometry two interfacial depth parameters, ξ, can be defined: for the y-direction $\xi^H = 2\gamma_0/H = 2\gamma_f/H_f$ and for the x-direction $\xi^W = 2x_0/W = 2x_f/W_f$. The interfacial depth parameters run between $0 < \xi^H, \xi^W < 1$ as well. The two interfacial depth parameters are assumed to be similar to each other, $\xi^H = \xi^W$; this assumption is later proved by the experimental results. Coupling Equations (18) and (19), Equation (20) derived.

$$\frac{V_z(\gamma_0, n)}{V_{swelled}} = \frac{2n+1}{n+1}\left[1 - \left(\xi^H\right)^{\frac{1}{n}+1}\right]\left(\frac{H'W'}{HW}\right) \tag{20}$$

The surface layer of the extrudate moves with $V_{extr.,surface}$, which can be estimated by

$$V_{extr.,surface} = \frac{Q_s}{HW - 2x_0 2\gamma_0} = \frac{Q_s}{HW(1 - \xi^W\xi^H)} = \frac{Q_s}{HW(1 - \xi^2)} \tag{21}$$

where Q_s is the flow rate of the surface layer and can be obtained by Equation (22).

$$Q_s = Q - 4\int_0^{\gamma_0}\int_0^{x_0} V_z \, dxd\gamma$$

$$= Q - 4\int_0^{\gamma_0}\int_0^{x_0}\left(\frac{2n+1}{n+1}\frac{Q}{HW}\left[1 - \left(\frac{2\gamma}{H}\right)^{\frac{1}{n}+1}\right]\right) dxd\gamma \rightarrow$$

$$Q_s = Q\left(1 - \left(\frac{2n+1}{n+1}\right)\xi^2 + \left(\frac{n}{n+1}\right)\xi^{3+\frac{1}{n}}\right) \tag{22}$$

For the detailed derivation of Equation (22), see Appendix B. Assuming that the fracture instability is formed on the surface layer of the extrudate, the ratio of the $V_{swelled}/V_{extr.,surface}$, (Equation (23)), is obtained by the coupling of Equations (18), (21), and (22).

$$\frac{V_{swelled}}{V_{extr.,surface}} = \frac{HW}{H'W'}(1 - \xi^2)\left[1 - \left(\frac{2n+1}{n+1}\right)\xi^2 + \left(\frac{n}{n+1}\right)\xi^{3+\frac{1}{n}}\right]^{-1} \tag{23}$$

Focusing on the die exit region the force balance for the slit die geometry is given by Equation (24).

$$Y_s\left(HW - 4x_0\gamma_0\right) = \sigma_x\lambda_s 2x_0 + \sigma_y\lambda_s 2\gamma_0 \tag{24}$$

Equation (24) presents the force balance between the shear stress σ_i on the interface between the core and surface layer, and the extensional stress Y_s at the die exit region for a slit die (rectangular cross-section area). The width of the instability ridge on the surface layer is λ_s, and it is assumed[17] to be the same for the x and y directions. The magnitude of the shear stress for both directions σ_x, σ_y is assumed to have a similar numerical value, $\sigma_x \approx \sigma_y$. Hence, the instability ridge, λ_s, is given by Equation (25).

$$\lambda_s = \frac{Y_s}{\sigma_x}\frac{(HW - 4x_0\gamma_0)}{2(x_0 + \gamma_0)} = \frac{Y_s}{\sigma_x}\frac{HW}{H+W}\left[\frac{1}{\xi} - \xi\right] \tag{25}$$

For the detailed derivation of Equation (25), see Appendix C. Using the assumption of Inn et al.[17] that the characteristic time periodicity τ of the instabilities is a constant ratio of $\tau = \lambda_s/V_{extr.,surface} = \lambda/V_{swelled}$, hence $\lambda = \lambda_s(V_{swelled}/V_{extr.,surface})$ occurs. Experimental data of the characteristic time periodicity τ of the extrusion instabilities can be obtained by high-sensitive pressure transducers within the slit die.[21,48–52] An analytical formula for the spatial characteristic wavelength, λ, is derived by coupling Equations (23) and (25) and $\lambda = \lambda_s(V_{swelled}/V_{extr.,surface})$, giving Equa-

**ADVANCED
SCIENCE NEWS**

www.advancedsciencenews.com

[M]acro-
olecular

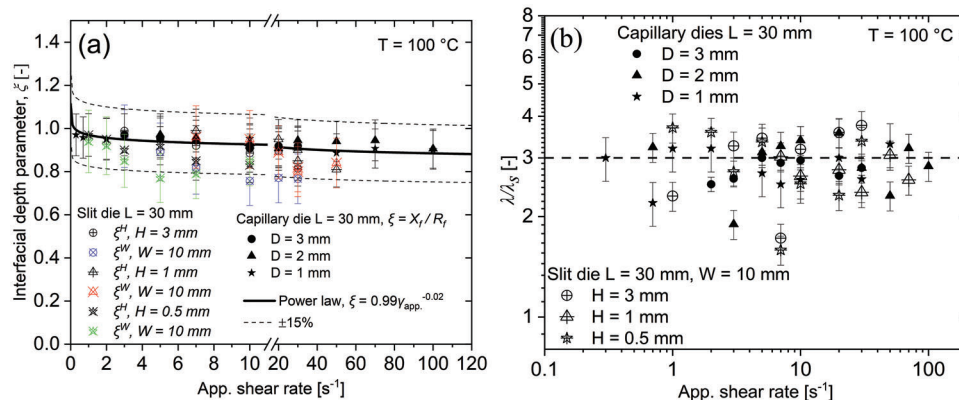Materials and Engineering

www.mame-journal.de

Figure 7. a) Experimental data of the calculated interfacial depth parameter ξ for extrudates obtained by round capillary and slit dies at $T = 100\,°C$. b) Ratio of the spatial characteristic wavelength and the instability ridge, $\lambda\lambda_s$, for the investigated sample obtained by capillary and slit dies at $T = 100\,°C$. The extrusion dies that have been used are: round capillary dies with $L = 30$ mm and $D = 1, 2,$ and, 3 mm and slit dies with $L = 30$ mm and $H = 0.5, 1,$ and 3 mm.

tion (26).

$$\lambda = \frac{Y_s}{\sigma_x} \frac{(HW)^2}{(H+W)\,H'W'} \left(\frac{1}{\xi} - \xi\right)\left(1 - \xi^2\right)$$

$$\times \left[1 + \left(\frac{2n+1}{n+1}\right)\xi^2 + \left(\frac{n}{n+1}\right)\xi^{3+\frac{1}{n}}\right]^{-1} \tag{26}$$

3.5. Simplification of the Models for Round Capillary and Slit Dies

In this section, the assumptions for the simplification of the models are experimentally validated. Firstly, the slip velocity is neglected because the model is derived directly at the die exit region, on the die lip. Secondly, the two interfacial depth parameters for the slit die geometry are assumed to be similar in magnitude to each other, $\xi^H \approx \xi^W$. Georgantopoulos et al.[22] proposed that the interfacial depth parameter ξ for extrudates obtained by capillary dies, for SBR materials can simply be described by a power law model as a function of apparent shear rate, $\xi = b\dot{\gamma}_{app.}^{-c}$. The apparent shear rate is defined as $\dot{\gamma}_{app.} = (6Q)/(WH^2)$ for slit dies and $\dot{\gamma}_{app.} = (4Q)/(\pi R^3)$ for round capillary dies. Based on the assumption of Inn et al.,[17] $R_f = X_f + h/2$, the same idea is applied for the extrudates obtained by the slit die, with $W_f = x_f + h/2$ and $H_f = y_f + h/2$. The experimental results for the interfacial depth parameter from extrudates obtained by slit and round capillary dies are presented in **Figure 7**a. Figure 7a shows that the interfacial depth parameter for the same material obtained by different die geometries remains similar to each other. The experimental data are fitted by the proposed[22] power law model, $\xi = b\dot{\gamma}_{app.}^{-c}$. The deviation of each experimental data obtained from different die geometries is estimated to vary at most by 15% from the fitting function. Hence, it is possible to assume that $\xi^H = \xi^W = \xi = b\dot{\gamma}_{app.}^{-c}$, where $b = 0.99$ s^{-c} and $c = 0.02$ for the investigated PBD sample at $T = 100\,°C$. The sensibility of the fitting parameters for the $\xi = b\dot{\gamma}_{app.}^{-c}$ is presented in Appendix D. According to Inn et al.[17] the ratio of the spatial characteristic wavelength λ and the instability ridge λ_s is given by $\frac{\lambda}{\lambda_s} = (V_{swelled}/V_{extr.,surface})$. Figure 7b presents experimental results obtained by slit and round capillary dies regard-

ing the ratio of the spatial characteristic wavelength λ and the instability ridge λ_s of the investigated PBD sample at $T = 100\,°C$. Within the investigated range of apparent shear rates, 0.5 s$^{-1} < \dot{\gamma}_{app.} < 100$ s^{-1} at $T = 100\,°C$, it is found that $\lambda/\lambda_s \approx 3$. It is worth mentioning that the ratio of the spatial characteristic wavelength λ and the instability ridge λ_s, has also been reported[22] that $\lambda/\lambda_s \approx 3$ for SBR samples, investigated at apparent shear rates in the range of, 1 s$^{-1} < \dot{\gamma}_{app.} < 100$ s^{-1} and $T = 120\,°C$.

Based on the previously reported assumptions which have been experimentally validated, Equations (27) and (28) are proposed as simplified qualitative models for the spatial characteristic wavelengths λ of extrusion flow instabilities developed at the die exit of round capillary and slit dies, respectively. The function for the interfacial depth parameter is given by $\xi = b\dot{\gamma}_{app.}^{-c}$, where $b = 0.99$ s^{-c} and $c = 0.02$ for the investigated PBD sample at $T = 100\,°C$.

$$\lambda_{Innetal.}^{Capillary} = 3\frac{R_0}{2}\left(\frac{Y_s}{\sigma_x}\right)\left(\frac{1}{\xi} - \xi\right) \tag{27}$$

$$\lambda_{currentwork}^{Slit} = 3\frac{HW}{H+W}\left(\frac{Y_s}{\sigma_x}\right)\left(\frac{1}{\xi} - \xi\right) \tag{28}$$

3.6. Predicting the Spatial Characteristic Wavelength from Round Capillary to Slit Dies and Vice Versa

Barone et al.[32] described the spatial characteristic wavelength λ of melt fracture for extrudates obtained by capillary dies as follows:

$$\lambda_{Barone\,et\,al.}^{Capillary} = \langle V\rangle\,\tau^* = \frac{D}{8}\left(\frac{\rho}{\rho'}\right)\left(\frac{D}{D'}\right)^2\dot{\gamma}_{app.}\tau^*. \tag{29}$$

where, $\langle V\rangle$ is the average extrudate velocity which is taking into account the swelled diameter D' of the extrudate, the density of the material inside the capillary reservoir ρ, and outside of the die ρ'. Georgantopoulos et al.,[21] used Equation (29) assuming the density ratio $\rho/\rho' \approx 1$ and similar extrusion conditions (temperature and deformation rates) between a round capillary and a
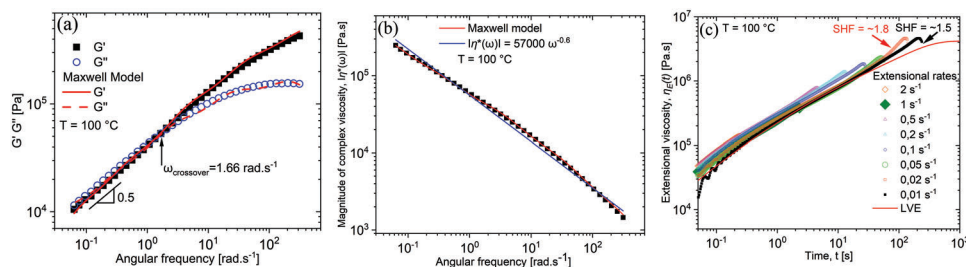
**ADVANCED
SCIENCE NEWS**

www.advancedsciencenews.com

**Macromolecular
Materials and Engineering**

www.mame-journal.de

Figure 8. a) Loss and storage moduli, b) magnitude of complex viscosity as a function of angular frequency fitted by a five-element Maxwell model, see also Appendix A. c) Transient extensional viscosity and the linear viscoelasticity (LVE).

slit die under the same apparent shear rate and temperature, that is:[21]

$$\dot{\gamma}_{app.}^{Capillary} = \dot{\gamma}_{app.}^{Slit} \Rightarrow \langle V \rangle^{Capillary} \left(\frac{D}{8} \right)^{-1} \left(\frac{D'}{D} \right)^2$$

$$= \langle V \rangle^{Slit} \left(\frac{H}{6} \right)^{-1} \left(\frac{H'}{H} \frac{W'}{W} \right). \quad (30)$$

Consistent with published optical[21] experimental observations, it is suggested that the swelling effect is similar between the round capillary and slit dies, $(D'/D)^2 \approx [(W'H')/(HW)]$ for the same material under similar process conditions (temperature and deformation rates). Moreover, it is experimentally validated[21] via three characterization techniques (online, offline optical analysis, and a customized highly sensitive pressure slit die) that the characteristic time periodicity τ^* of the extrusion flow instabilities is not die geometry dependent but material dependent. Fitting the experimental results, it is suggested[21] that the characteristic time periodicity τ^* can be simply modeled by a power law function,

$$\tau^* = a\dot{\gamma}_{app.}^{-d} \quad (31)$$

where a and d are fitting parameters and dependent on material properties.[21]

Based on Equation (30), the observation $(D'/D)^2 \approx [(W'H')/(HW)]$ and the material dependent characteristic time periodicity τ^*, the following geometrical model was proposed by the authors of this article in a previous publication,[21]

$$\lambda^{Slit} = \lambda_{Baroneetal.}^{Capillary} \left(\frac{8H}{6D} \right). \quad (32)$$

4. Results and Discussion

In **Figure 8**a,b, the small amplitude oscillatory shear (SAOS) experiments within the linear viscoelastic (LVE) region at $\gamma_0 = 1\%$ present the loss ($G''(\omega)$) modulus, storage ($G'(\omega)$) modulus, and the magnitude of complex viscosity ($|\eta^*(\omega)|$) as a function of angular frequency (ω). These material functions were obtained at $T = 100$ °C between angular frequency of $\omega = 0.06$ and 300 rad s^{-1}, and fitted by a five-element Maxwell model, see Appendix A. The investigated PBD sample has not reached the terminal flow zone ($\omega < \omega_{crossover}, \omega_{crossover} = 1.66$ rad s^{-1} where $G''\omega^1$ and $G'\omega^2$, see Figure 8a). Rather, the loss modulus ($G''(\omega)$) has slightly

higher values than storage ($G'(\omega)$) modulus and both of them scale similarly with the angular frequency, $G''G'\omega^{0.5}$. This scaling law behavior, $G''G'\omega^{0.5}$, indicates Rouse dynamics and it is observed in the literature[40–43] for comb-like molecular architectures. Within this study, this unusual behavior of the G'' and G' is explained based on the polydispersity ($Ð = 3.5$) of the investigated sample as well as on the literature explanation[40–43] from the presence of entanglements between the backbone and the branches. Those entanglements have a particularly long relaxation process since they relax during or even after the reptation of the macromolecular chain, which makes them considered "permanent" entanglements.[40–43] Hence, even after the crossover ($\omega_{crossover} = 1.66$ rad s^{-1}) the terminal regime is not reached because the polymeric chains are not fully relaxed due to the existence of "permanent" entanglements between the backbone and the branches.

As displayed in Figure 8b, the investigated PBD has a common power law ($|\eta^*(\omega)| = K\omega^{n-1}$) viscosity behavior, with $K = 57\,000$ Pa s^n and $n = 0.4$. Figure 8c displays the non-linear transient extensional viscosity investigated by the EVF at $T = 100$ °C. Within the investigated extensional rates, the data overlapped with the linear viscoelasticity (LVE), and indications of a minor strain hardening factor (SHF) are observed at $\dot{\varepsilon} = 0.01$ and 0.02 s^{-1}, SHF = 1.5 and 1.8 respectively. This indicates that the investigated PBD sample has a dominant linear molecular architecture with a possible additional low amount of branching at the high molecular weight tail of the MWD.[22] This molecular architecture agrees with the experimental results from Mark–Houwink plot ((Figure 1b) and the theoretical explanation for the behavior of loss ($G''(\omega)$) and storage ($G'(\omega)$) modulus in Figure 8a.

Figure 9a,b displays the apparent steady-state viscosity ($\eta_{app.}$) as a function of the apparent shear rate ($\dot{\gamma}_{app.}$) for the slit and round capillary extrusion dies, respectively. The apparent steady-state viscosity was obtained at $T = 100$ °C between $\dot{\gamma}_{app.} = 0.7$ and 1000 s^{-1} for the slit dies (Figure 9a) and $\dot{\gamma}_{app.} = 0.1$ to 1000 s^{-1} for the capillary dies (Figure 9b). The zero-shear viscosity (η_0) is obtained by steady shear experiments using the ARES-G2 strain-controlled rheometer between $\dot{\gamma}_{app.} = 0.004$ and 0.05 s^{-1} at $T = 100$ °C. The experimental data are fitted by the Cross model, Equation (2), where $\eta_0 = 750$ kPa s, $\tau = 6$ s, and $m = 0.92$. A deviation between the apparent steady-state viscosity obtained by different dies is observed. This deviation is caused by the exit pressure effects and slippage behavior on the die wall. The exit pressure effect on the steady-state viscosity obtained by the slit die with an aspect ratio of $L/H = 60$ and $H = 0.5$ mm, can be neglected due to the large aspect ratio.[44] Hence, the obtained apparent steady-state viscos-
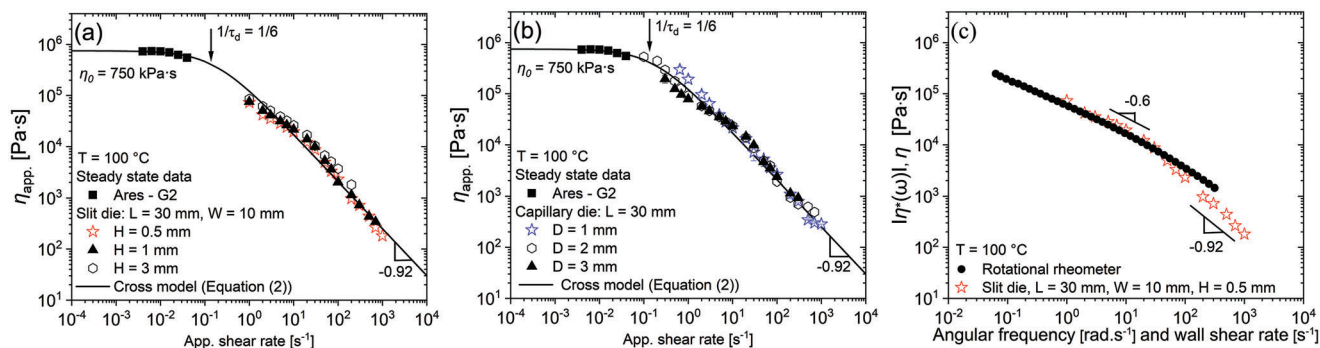
Figure 9. a–b) Apparent steady state viscosity as a function of apparent shear rate for the slit and capillary die geometries, respectively. The experimental data are fitted by the Cross model, Equation (2). c) Comparison between the magnitude of complex viscosity obtained by oscillatory shear experiment (black solid circles) and the steady state viscosity (red open stars) obtained by capillary rheology with a slit die $L/H = 60$, and $H = 0.5$ mm. All the experiments were carried out at $T = 100$ °C.
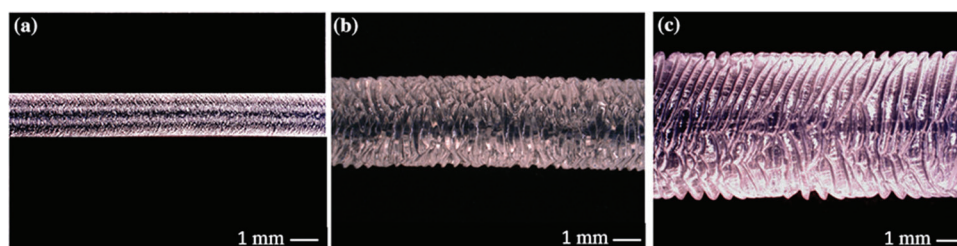
Figure 10. Images of the extruded PBD sample with capillary dies a) $D = 1$ mm, b) $D = 2$ mm, c) $D = 3$ mm, and $L = 30$ mm at $T = 100$ °C and $\dot{\gamma}_{app.} = 5$ s^{-1}.

ity $\eta_{app.}$ (or apparent shear stress $\sigma_{app.}$) is the correct steady-state viscosity η (or wall shear stress σ_{wall}) without requiring a Bagley correction.[4] For this reason, the Rabinowitsch–Weissenberg[4] correction, where the $\dot{\gamma}_{wall} = [(2n + 1)/3n]\dot{\gamma}_{app.}$ and n is defined by the $n \equiv d(log\sigma_{wall})/d(log\dot{\gamma}_{app.})$, can directly be applied. Thus, the Cox–Merz rule[39] is applied in Figure 9c, where the magnitude of complex viscosity as a function of angular frequency and the steady state viscosity as a function of wall shear rate is presented in the same plot. The Cox–Merz[39] rule is applicable between $1\ s^{-1} < \dot{\gamma}_{wall} < 50\ s^{-1}$ where both viscosities overlap, after $\dot{\gamma}_{wall} > 50\ s^{-1}$ the steady state viscosity scales with the slope of -0.92 and deviates from the magnitude of complex viscosity. This deviation has been discussed in the literature and explained based on the intensive slippage on the extrusion die wall.[21,45–48]

Figure 10 presents the images of the extrudates obtained by three round capillary dies, with $D = 1, 2$, and 3 mm, and $L = 30$ mm at the same shear rate, $\dot{\gamma}_{app.} = 5\ s^{-1}$, and temperature, $T = 100$ °C. The spatial characteristic wavelength λ of the presented melt fracture can be identified. It is obvious that the absolute value of the spatial characteristic wavelength λ becomes bigger as the diameter of the die increases. This observation agrees with the literature experimental results for polyethylene samples by Wang and coworkers.[30–32]

Optical microscopy was used to quantify the spatial characteristic wavelength λ. The numerical values of the spatial characteristic wavelength λ are presented in **Figure 11**a. The data which are marked by a shaded area, Figure 11a, are obtained by the stick part of the stick-slip instability. These experimental results are fitted by the Inn et al.[17] model, Equation (27), and the magni-

tude of the stress ratio Y_s/σ_x is obtained. The Inn et al.[17] model has agreement with the experimental data both qualitatively and quantitatively. The stress ratio Y_s/σ_x as a function of the diameter D of the capillary dies is presented in Figure 11b. It is observed that the stress ratio Y_s/σ_x is slightly decreased as the diameter D of the capillary die increases.

In **Figure 12**, images of the extrudates obtained by the three slit dies, with $H = 0.5$ mm, $H = 1$ mm and $H = 3$ mm, and $L = 30$ mm at $T = 100$ °C are presented. The spatial characteristic wavelength λ of the instability can be identified. The absolute value of the spatial characteristic wavelength λ becomes bigger as the height H of the die increases, which is a similar behavior with the extrudates from capillary dies.

The numerical values of the spatial characteristic wavelength λ are presented in **Figure 13**a. The experimental data of the wavelength are fitted by the proposed model from this study, see Equation (28). The spatial characteristic wavelength λ obtained by the stick part (marked data in Figure 13a) of the stick-slip instability is reasonably described by the proposed model as well. The magnitude of the stress ratio Y_s/σ_x is also obtained as well. The proposed model agrees with the experimental data and has similar behavior of the Inn et al.[17] model. The stress ratio Y_s/σ_x as a function of the height H of the slit die is presented in Figure 13b. It is also noticed that the stress ratio Y_s/σ_x decreases as the height H of the slit die increases.

The obtained stress ratios Y_s/σ_x through the model fitting, Equations (27) and (28), confirm the assumption[21] that the extensional stress on the surface layer of the extrudate at the die exit region is larger than the theoretical shear stress on the interface
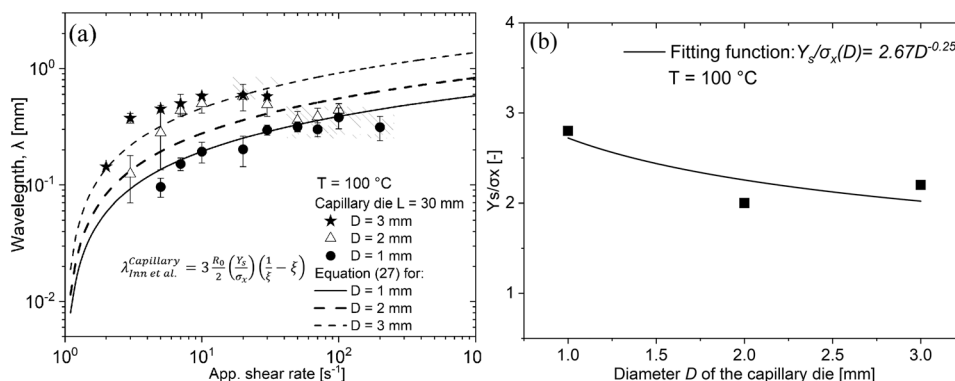
Figure 11. a) Spatial characteristic wavelength λ obtained by capillary dies with $D = 1$ mm, $D = 2$ mm, $D = 3$ mm, and $L = 30$ mm. The experimental data are fitted by the Inn et al.[17] model, Equation (27). The data marked by the shaded area were obtained at the stick part of the stick-slip instability, see Figure 3b. b) The stress ratio Y_s/σ_x at the die exit region as a function of the diameter D of the capillary die.
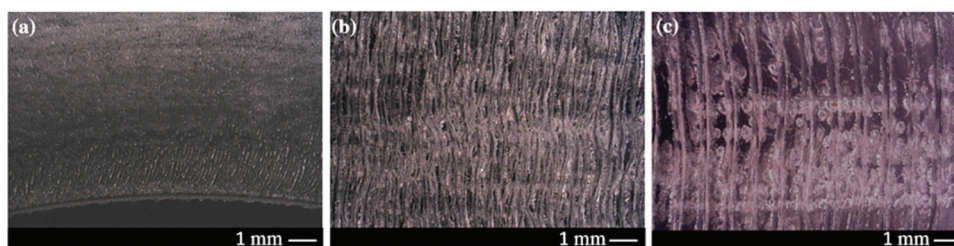

Figure 12. Images from the extruded PBD from slit dies with a) $H = 0.5$ mm, b) $H = 1$ mm, c) $H = 3$ mm, and $L = 30$ mm at $T = 100$ °C and $\dot{\gamma}_{app.} = 10$ s^{-1}.

between the two layers (surface and core), $Y_s > \sigma_x$. An interesting topic would be the evaluation of the magnitude of the stress ratio Y_s/σ_x via computational fluid dynamic (CFD) simulation at the die exit region. Taking into account the universality of the discussed models at the die exit area and excluding localized discontinuities at the die exit corner, insights for the ratio of the stress Y_s/σ_x can be found possibly. The downward behavior of the stress ratio Y_s/σ_x as the characteristic dimension of the die increases is explained based on the theoretical core layer of the extrudate

which is increasing as well. For instance, during the same applied apparent shear rate, the extrudate velocity ($V_{extr.}^{Capillary} = (D/8)\dot{\gamma}_{app.}$, $V_{extr.}^{Slit} = (H/6)\dot{\gamma}_{app.}$) is increased as the height H or the diameter D of the die increases. Thus, the mass flux of the theoretical cross-section area of the core layer is increased as the characteristic dimension of the die increases.

In **Figure 14**, the slit-die-simple-profile is displayed, see also Figure 2a. Specifically, in Figure 14a„ the cross-section area of the die exit is presented, giving numerical values for selective di-
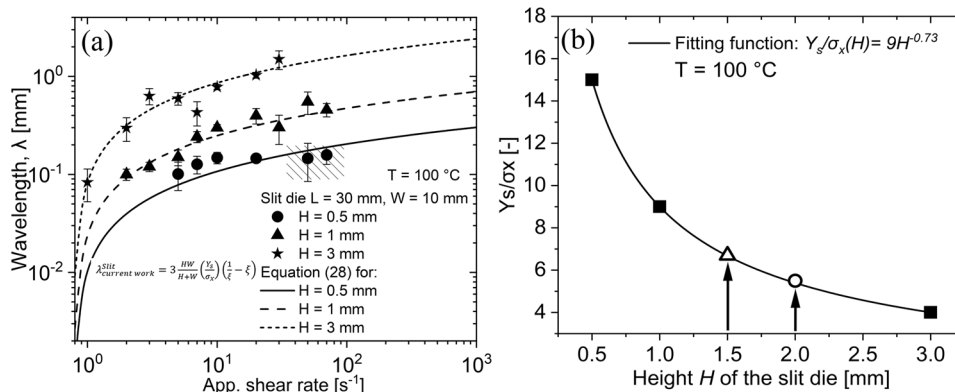

Figure 13. a) Spatial characteristic wavelength λ obtained by slit dies with $H = 0.5$ mm, $H = 1$ mm, $H = 3$ mm, $W = 10$ mm and $L = 30$ mm. The experimental data are fitted by the proposed model, Equation (28). b) The ratio of the stress Y_s/σ_x at the die exit region as a function of the height H of the die. The solid symbols are obtained by fitting Equation (28) to the experimental data. The open triangle and circular symbols are estimating the Y_s/σ_x for the $H = 1.5$ mm and $H = 2$ by using the fitting line. This information will later be input to Equation (28) in order to predict the spatial characteristic wavelength for the respective height.
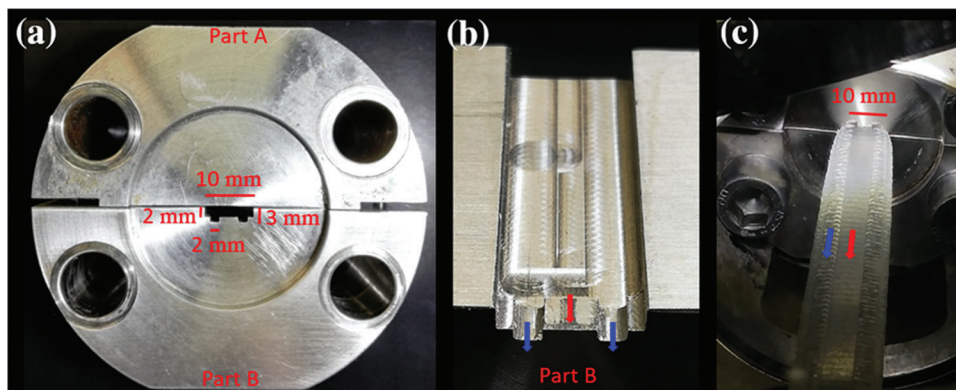
www.advancedsciencenews.com

[M]acro-molecular
Materials and Engineering
www.mame-journal.de

Figure 14. Slit-die-simple-profile. a) The cross-section area, b) the flow channel part, where the profile is existing at the last $L_{profile} = 3$ mm of the die exit, and c) visualization of the flow during extrusion of the investigated PBD at $T = 100$ °C, $\dot\gamma_{app.}^{H=2mm} = 10$ s^{-1} and $\dot\gamma_{app.}^{H=3mm} = 11.11$ s^{-1}. The computer-aided design (CAD) drawings can be found in the supplementary information. In b) the milling process fingerprint can be noted. The die land surface has been polished and major roughness from the milling process has been removed.
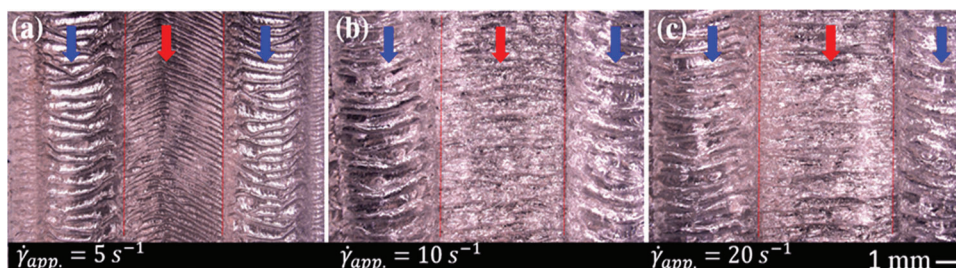

Figure 15. Images of the extruded PBD from slit-die-simple-profile (Figures 2 and 14a) at a) $\dot\gamma_{app.}^{H=2mm} = 5$ s^{-1} and $\dot\gamma_{app.}^{H=3mm} = 5.5$ s^{-1}, b) $\dot\gamma_{app.}^{H=2mm} = 10$ s^{-1} and $\dot\gamma_{app.}^{H=3mm} = 11.11$ s^{-1}, and c) $\dot\gamma_{app.}^{H=2mm} = 20$ s^{-1}, and $\dot\gamma_{app.}^{H=3mm} = 22.22$ s^{-1} at $T = 100$ °C. The arrows indicate the flow direction, the red arrow represents the flow at the die section with $H = 2$ mm and the blue arrows at the die section with $H = 3$ mm.

mensions of the profile. Figure 14b presents the flow channel and the die exit region with the profile. The flow channel is $L = 30$ mm and the profile for the die exit region has a length of $L_{profile} = 3$ mm within the flow channel. The arrows indicate the flow direction: blue arrows for the flow at $H = 3$ mm and red at $H = 2$ mm. The shear rates $\dot\gamma_{app.} = (6Q)/(WH^2)$ for the respective height of the slit-die-simple-profile are presented in Table S4, Supporting Information. In Figure 14c an image during the extrusion of the investigated PBD sample at $T = 100$ °C, $\dot\gamma_{app.}^{H=2mm} = 10$ s^{-1}, and $\dot\gamma_{app.}^{H=3mm} = 11.11$ s^{-1} is depicted. During the extrusion process, the two different spatial wavelength λ regimes can be easily identified. **Figure 15** presents selected extrudates obtained by the slit-die-simple-profile at $T = 100$ °C. On all of the extrudates, red and blue arrows indicate the extrusion area where the height of the slit die is $H = 2$ mm and $H = 3$ mm, respectively. The spatial characteristic wavelength λ obtained for the area where the height is $H = 3$ mm (blue arrows) is visually confirmed that is bigger than the wavelength λ obtained from the $H = 2$ mm (red arrow).

In **Figure 16** the spatial characteristic wavelength λ obtained by the slit die with $H = 3$ mm, $W = 10$ mm and $L = 30$ mm and the slit-die-simple-profile with $L = 30$ mm, $W = 10$ mm and $H = 2$ and 3 mm are presented. The numerical values of the wavelength obtained by the slit die ($H = 3$ mm) and the section with $H = 3$ mm from the slit-die-simple-profile are overlapping. In addition, the wavelength obtained at the section with $H = 2$ mm from
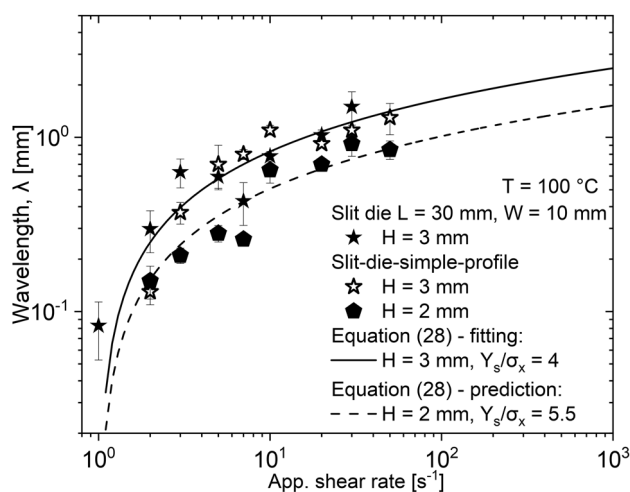

Figure 16. Spatial characteristic wavelength λ obtained by slit die with $H = 3$ mm (solid star symbol) and by slit-die-simple-profile (Figure 13a) with $H = 3$ mm (open star symbol) and $H = 2$ mm (solid pentagon symbol). The apparent shear rate is calculated by $\dot\gamma_{app.} = (6Q)/(WH^2)$ and the numerical values of it can be found in the supplementary information.

the slit-die-simple-profile has lower numerical values. The proposed model, Equation (28), is used to fit the experimental data of the wavelength obtained by the slit die and the slit-die-simple-
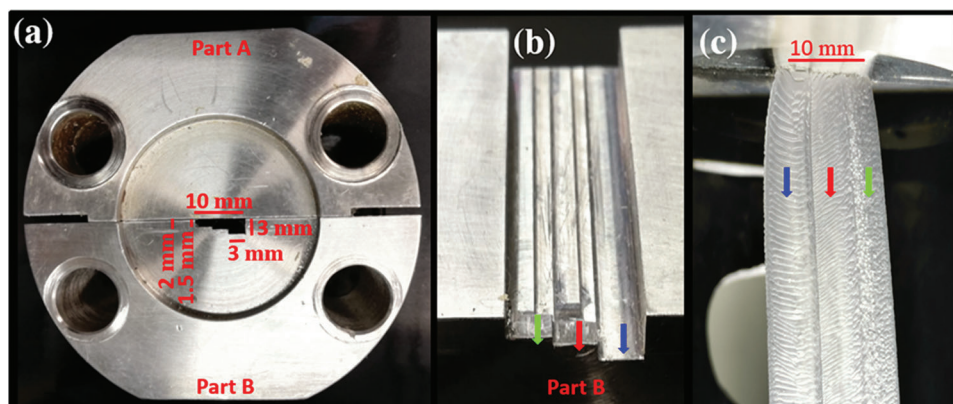
**ADVANCED
SCIENCE NEWS**
www.advancedsciencenews.com

{M} **acro-
olecular
Materials** and **Engineering**
www.mame-journal.de

Figure 17. Slit-die-scalar-profile. a) The cross-section area, b) the flow channel part, where the profile is existing at the last $L_{profile}$ = 3 mm of the die exit, and c) visualization of the flow during extrusion of the investigated PBD at $\dot{\gamma}_{app.}^{H=1.5mm}$ = 106 s^{-1}, $\dot{\gamma}_{app.}^{H=2mm}$ = 20 s^{-1}, and $\dot{\gamma}_{app.}^{H=3mm}$ = 26.7 s^{-1} and T = 100 °C. The computer-aided design (CAD) drawings can be found in the supplementary information.
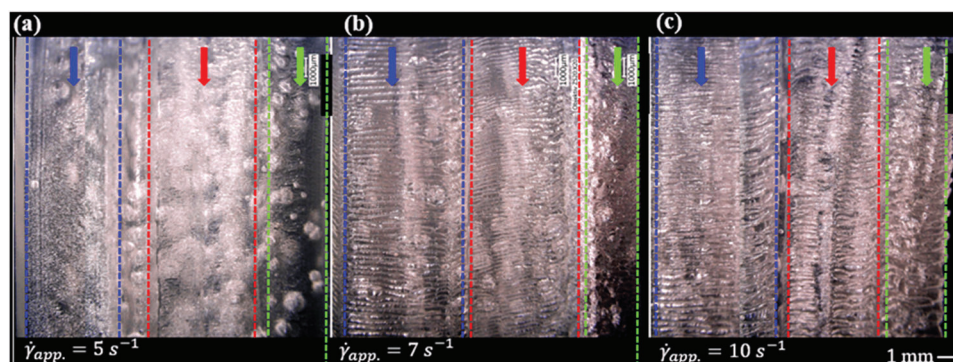

Figure 18. Images from the extruded PBD from slit-die-scalar-profile (Figures 2b and 17a) at a) $\dot{\gamma}_{app.}^{H=1.5mm}$ = 26.7 s^{-1}, $\dot{\gamma}_{app.}^{H=2mm}$ = 5 s^{-1} and $\dot{\gamma}_{app.}^{H=3mm}$ = 6.7 s^{-1}, b) $\dot{\gamma}_{app.}^{H=1.5mm}$ = 37.3 s^{-1}, $\dot{\gamma}_{app.}^{H=2mm}$ = 7 s^{-1} and $\dot{\gamma}_{app.}^{H=3mm}$ = 9.3 s^{-1}, c) $\dot{\gamma}_{app.}^{H=1.5mm}$ = 53.3 s^{-1}, $\dot{\gamma}_{app.}^{H=2mm}$ = 10 s^{-1}, and $\dot{\gamma}_{app.}^{H=3mm}$ = 13.3 s^{-1} at T = 100 °C. The arrows indicate the flow direction, the green arrow represents the flow at the die section with H = 1.5 mm, the red arrow at H = 2 mm and the blue arrow at H = 3 mm.

profile with H = 3 mm. The numerical values of the wavelength obtained by the slit-die-simple-profile with H = 2 mm are predicted by Equation (28) estimating the stress ratio Y_s/σ_x = 5.5 from Figure 13b and using $\xi = 0.99\dot{\gamma}_{app.}^{-0.02}$.

In **Figure 17** the slit-die-scalar-profile is presented. In Figure 17a, the cross-section area of the die exit is presented, giving numerical values for selective dimensions. This design of the slit-die-scalar-profile is inspired by industrial dies which are used in the automotive industry.[38] Figure 17b displays the flow channel with the profile of the cross-section area. The flow channel is L = 30 mm and the profile for the die exit region has a length of $L_{profile}$ = 3 mm within the flow channel. The arrows indicate the flow direction, the blue arrows represent the flow at H = 3 mm, the red arrows at H = 2 mm, and the green arrow at H = 1.5 mm. In Figure 17c, an image during the extrusion of the investigated PBD sample at T = 100 °C and $\dot{\gamma}_{app.}^{H=1.5mm}$ = 106 s^{-1}, $\dot{\gamma}_{app.}^{H=2mm}$ = 20 s^{-1} and $\dot{\gamma}_{app.}^{H=3mm}$ = 26.7 s^{-1} is depicted. During the extrusion process, the three different spatial wavelength λ regimes can be identified.

Figure 18 presents selected extrudates obtained by the slit-die-scalar-profile at T = 100 °C. On the extrudates surface blue, red, and green arrows indicate the flow where the height of the slit

die is H = 3 mm, H = 2 mm, and H = 1.5 mm, respectively. The spatial characteristic wavelength λ can be visually identified that is bigger at H = 3 mm (blue arrow) and smaller at H = 1.5 mm (green arrow).

In **Figure 19** the 3D surface profiles of the extruded PBD from three different dies: a) slit die, b) slit-die-simple-profile, and c) slit-die-scalar-profile at T = 100 °C are presented. The escalation of the spatial characteristic wavelength λ within Figure 19b,c is easily visible at the different height levels of the profile.

In **Figure 20**, the magnitude values of the spatial characteristic wavelength λ obtained by the slit die with L = 30 mm, W = 10 mm, H = 3 mm, the slit-die-simple-profile with L = 30 mm, W = 10 mm, H = 2 and 3 mm, and the slit-die-scalar-profile with L = 30 mm, W = 10 mm and H = 1.5, 2 and 3 mm are presented. The shear rates $\dot{\gamma}_{app.}$ = $(6Q)/(WH^2)$ for the respective height of the slit-die-scalar-profile are presented in Table S5, Supporting Information. In Figure 20a, the numerical values of the wavelength obtained by the slit die (H = 3 mm), the slit-die-simple-profile section with H = 3 mm, and the slit-die-scalar-profile section with H = 3 mm are overlapping. In Figure 20b, the numerical values of the wavelength obtained by the slit-die-simple-profile sec-
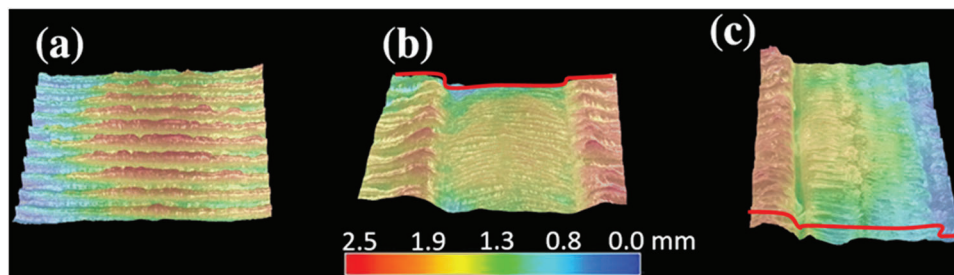
**ADVANCED
SCIENCE NEWS**

www.advancedsciencenews.com

acro-
olecular
Materials and Engineering
www.mame-journal.de

Figure 19. The 3D profiles of the extrudates obtained by a) slit die with $H = 3$ mm, $W = 10$ mm at $\dot{\gamma}_{app.}^{H=3mm} = 7$ s^{-1}, b) slit-die-simple-profile with $H = 3$ mm, $H = 2$ mm, $W = 10$ mm, at $\dot{\gamma}_{app.}^{H=2mm} = 7$ s^{-1}, $\dot{\gamma}_{app.}^{H=3mm} = 7.7$ s^{-1}, and c) slit-die-scalar-profile with $H = 3$ mm, $H = 2$ mm, $H = 1.5$ mm and $W = 10$ mm, at $\dot{\gamma}_{app.}^{H=1.5mm} = 37.3$ s^{-1}, $\dot{\gamma}_{app.}^{H=2mm} = 7$ s^{-1}, and $\dot{\gamma}_{app.}^{H=3mm} = 9.3$ s^{-1}, see Figures 2, 14, and 17 for the dies. All the dies have a length of $L = 30$ mm and the profile for the b–c) is existing at $L_{profile} = 3$ mm before the die exit. The extrudate was obtained at $T = 100$ °C.
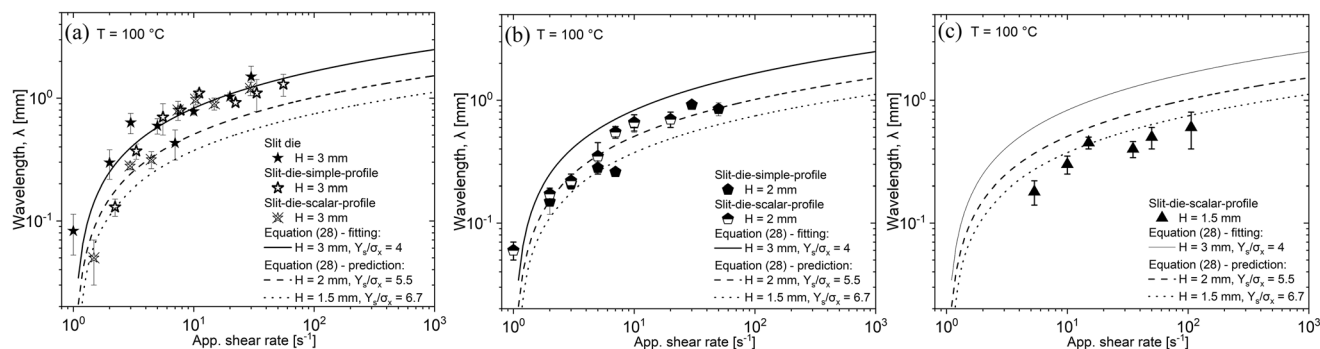

Figure 20. Spatial characteristic wavelength λ obtained a) by slit die with $H = 3$ mm (solid star symbol), slit-die-simple-profile (Figure 14a) with $H = 3$ mm (open star symbol) and slit-die-scalar-profile (Figure 17a) with $H = 3$ mm (semi-open star symbol). b) Wavelength obtained by slit-die-simple-profile with $H = 2$ mm (solid pentagon symbol) and slit-die-scalar-profile with $H = 2$ mm (semi-open pentagon symbol). c) Wavelength obtained by slit-die-scalar-profile with $H = 1.5$ mm (solid triangle symbol). The solid lines are the fitting of Equation (28) to the experimental data obtained by the slit die with $H = 3$ mm. The dash and dot lines are predictions of Equation (28) for the $H = 2$ mm and $H = 1.5$ mm. The choice of the ratio of the stress Y_s/σ_x for the $H = 2$ mm and $H = 1.5$ mm has been based on Figure 13b. The fitting and the predictions of Equation (28) are included in all the figures to emphasize the difference between the heights. The apparent shear rate is calculated by $\dot{\gamma}_{app.} = (6Q)/(WH^2)$ and the numerical values of it can be found in the supplementary information.

tion with $H = 2$ mm, and the slit-die-scalar-profile section with $H = 2$ mm are overlapping as well. Finally, in Figure 20c, the numerical values of the wavelength obtained by the slit-die-scalar-profile section with $H = 1.5$ mm are presented. The proposed model, Equation (28), is used to fit the experimental data of the wavelength obtained by the slit die with $H = 3$ mm, using $Y_s/\sigma_x = 4$ and $\xi = 0.99\dot{\gamma}_{app.}^{-0.02}$. Based on Figure 13b the ratio of Y_s/σ_x can be estimated of $Y_s/\sigma_x = 5.5$ for $H = 2$ mm and $Y_s/\sigma_x = 6.7$ for $H = 1.5$ mm. Using the estimated values for the Y_s/σ_x and $\xi = 0.99\dot{\gamma}_{app.}^{-0.02}$, predictions of Equation (28) are included in Figure 20. In Figure 20b,c, the comparison between the predictions of Equation (28) and the experimental data obtained by $H = 2$ mm and $H = 1.5$ mm are presented. Agreement between the predictions and the experimental data is observed.

The prediction of the spatial characteristic wavelength λ of the extrusion flow instabilities for a given material from a round capillary die, which usually exists in a laboratory, to industrial-scale slit dies can be a useful and practical tool for the plastic and rubber processing industry. A geometrical correlation, Equation (32), between the spatial characteristic wavelengths λ of extrudates obtained by capillary and slit dies is proposed in the literature.[21] Equation (32) has been tested for two SBR samples extruded by

a capillary die $D = 2$ mm, $L = 30$ mm and a slit die with $H = 0.5$ mm, $W = 5$ mm, and $L = 30$ mm at $T = 120$ °C.[21] The predictions of Equation (32) for the spatial characteristic wavelength λ as obtained by the slit die are in agreement with the experimental data. Within this study, the validity of Equation (32) for the prediction of the spatial characteristic wavelengths λ for three different slit dies with $H = 0.5$, 1, and 3 mm at $T = 100$ °C is examined. Firstly, the experimental results of the spatial characteristic wavelength λ obtained by the round capillary die with $D = 2$ mm, and $L = 30$ mm are fitted by the Barone et al.[33] model (Equation (29)), see **Figure 21**a. The density ratio ρ/ρ' for the investigated PBD sample is assumed to be $\rho/\rho' \approx 1$, the swelled ratio is $(D/D')^2 = 0.28$, and the time periodicity[49–52] of the phenomenon is given by $\tau^* = 1.6\dot{\gamma}_{app.}^{-0.5}$ at $T = 100$ °C. The marked experimental results in Figure 21a, between 50 s$^{-1} \leq \dot{\gamma}_{app.} \leq 100$ s^{-1}, are excluded from the fitting of the Barone et al.[33] model. Those experimental data were obtained by the stick part of the stick-slip instability. Barone et al.[33] developed their model based on visual observations of a specific linear low-density polyethylene (LLDPE, $M_w = 112$ kg mol^{-1}, $Đ = 4.15$) with pronounced sharkskin instability. For this reason, only the data associated with the sharkskin instability are fitted by Barone et al.[33] in Figure 21a. Using the Barone et al.[33]
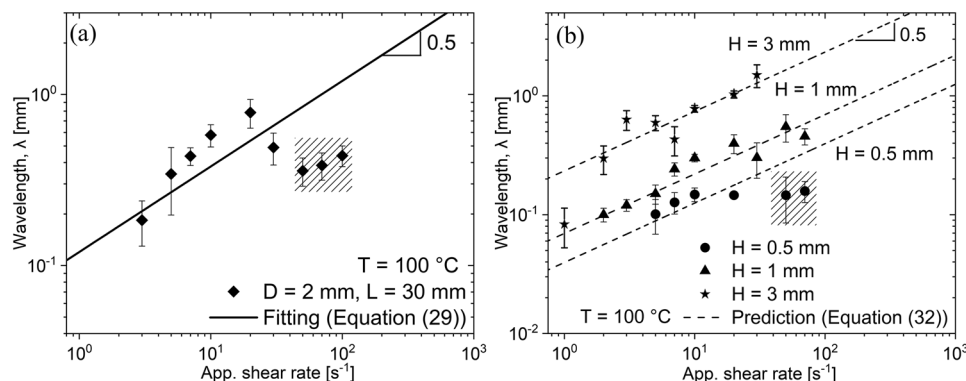
Figure 21. a) Spatial characteristic wavelength λ obtained by capillary dies with $D = 2$ mm, $L = 30$ mm and fitted by the Barone et al.[33] model, Equation (29). b) Spatial characteristic wavelength λ obtained by slit dies $H = 0.5$ mm, $H = 1$ mm, $H = 3$ mm, with $L = 30$ mm, and predicted by the proposed correlation, Equation (32). The marked experimental data in (a) and (b) are obtained by the stick part of the stick-slip instability.

model which fitted the experimental results from the round capillary die $D = 2$ mm, $L = 30$ mm, and knowing the different heights of slit dies $H = 0.5$, 1, and 3 mm, the predictions of Equation (32) are presented in Figure 21b. The predictions of Equation (32) are in agreement with the experimental data obtained by the slit dies at $T = 100\,°C$. The deviation between the prediction and the experimental data is observed for the spatial characteristic wavelength obtained by the stick part of the stick-slip instability using the slit die with $H = 0.5$ mm.

5. Conclusion

Within this study, the rheological properties and the extrusion behavior of a commercial polybutadiene sample (PBD, $M_w = 610$ kg mol^{-1}, $Đ = 2.95$) were investigated using different round capillary and slit extrusion dies. The Inn et al.[17] model for the spatial characteristic wavelength λ for extrudates obtained by round capillary dies was used to fit the experimental data obtained by three round dies with $D = 1, 2, 3$ mm and $L = 30$ mm. The extensional and stress ratio Y_s/σ_x at the die exit region was obtained and correlated with the diameter D of the round capillary dies. Based on the Inn et al.[17] methodology and Ovaici et al.[34] for the force balance at the die exit region a new model for the spatial characteristic wavelength λ for extrudates obtained by slit dies was developed, see Equation (28) ($\lambda_{currentwork}^{Slit} = 3 \frac{HW}{H+W}(\frac{Y_s}{\sigma_x})(\frac{1}{\xi} - \xi)$). This new model was used to fit experimental data obtained by three slit dies with $L = 30$ mm, $W = 10$ mm, and $H = 0.5$, 1, and 3 mm. The extensional and shear stress ratio Y_s/σ_x at the die exit region was obtained and correlated with the height of the slit dies. For both the Inn et al.[17] model (Equation (27) ($\lambda_{Innetal.}^{Capillary} = 3 \frac{R_0}{2}(\frac{Y_s}{\sigma_x})(\frac{1}{\xi} - \xi)$)) and the newly proposed model (Equation (28)), the same behavior between the shear stress ratio Y_s/σ_x and the characteristic dimension (diameter D, and height H) of the extrusion die was observed. The magnitude of the stress ratio Y_s/σ_x decreased as the characteristic dimension of the die was increased. The new qualitative model for slit die geometry was used and predicted the spatial characteristic wavelength λ of the extrudates obtained by the slit-die-simple-profile and slit-die-scalar-profile. Moreover, the recently proposed correlation by our group[21] for the prediction of the spatial characteristic wavelength λ from a capillary die to several slit dies was found to be valid for the investigated sample and die geometries.

Appendix A

Table A1. Maxwell modes of the investigated polybutadiene at 100 °C.

Modes	λ_i [s]	G_i [kPa]
1	23 160	13,24
2	2670	23,37
3	0310	84,14
4	0035	182,20
5	0004	275,60

Appendix B

Derivation of the volumetric flow rate of the surface layer of the extrudate.

$$Q_s = Q - 4 \int_0^{y_0}\int_0^{x_0} V_z\, dx dy = Q - 4 \int_0^{y_0}\int_0^{x_0}\left(\frac{2n+1}{n+1}\frac{Q}{HW}\left[1 - \left(\frac{2y}{H}\right)^{\frac{1}{n}+1}\right]\right) dxdy \rightarrow$$

$$Q_s = Q - 4\frac{2n+1}{n+1}\frac{Q}{HW}\int_0^{y_0}\left[1 - \left(\frac{2y}{H}\right)^{\frac{1}{n}+1}\right] dy \rightarrow$$

$$Q_s = Q - 4\frac{2n+1}{n+1}\frac{Q}{HW}x_0\left[y_0 - \left(\frac{2}{H}\right)^{1+\frac{1}{n}}\frac{n}{1+2n}y_0^{2+\frac{1}{n}}\right] \rightarrow$$

$$\frac{Q_s}{Q} = 1 - \frac{2n+1}{n+1}\xi^2 + \frac{n}{n+1}\xi^{3+\frac{1}{n}} \tag{A1}$$

Appendix C

Derivation of Equation (25) from Equation (24):

$$\lambda_s = \frac{Y_s}{\sigma_x}\frac{(HW - 4x_0 y_0)}{2(x_0 + y_0)} \rightarrow \lambda_s = \frac{Y_s}{\sigma_x}\frac{\left(\frac{HW}{HW} - \frac{4x_0 y_0}{HW}\right)}{\frac{2(x_0 + x_0)}{HW}} \rightarrow$$

$$\lambda_s = \frac{Y_s}{\sigma_x}\left[\frac{1 - \xi^2}{\frac{2x_0}{HW} + \frac{2y_0}{HW}}\right] \rightarrow \lambda_s = \frac{Y_s}{\sigma_x}\frac{HW}{W+H}\left[\frac{1}{\xi} - \xi\right] \tag{A2}$$
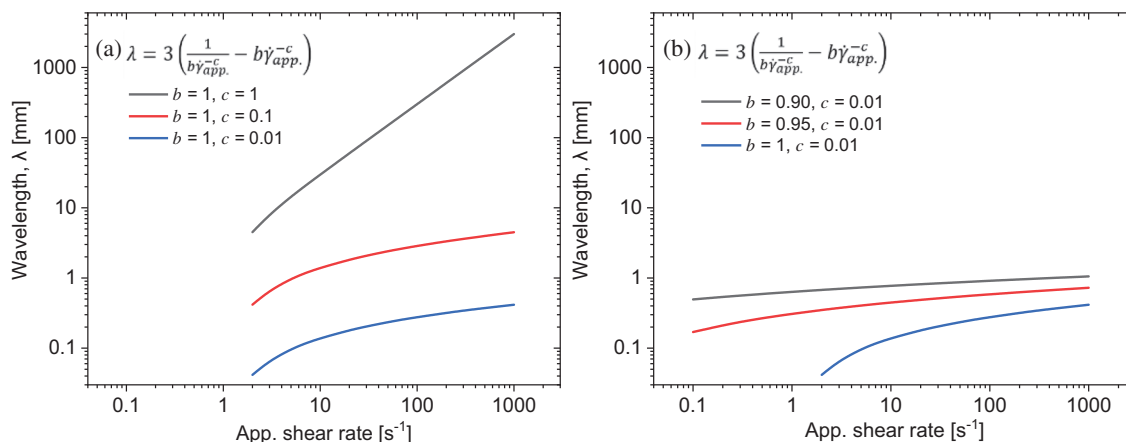
Figure D1. Parameterization of the fitting parameters a) c and b) b for the suggested model of the interfacial depth parameter $\xi = b\dot{\gamma}_{app.}^{-c}$.

Appendix D

Using the model of Inn et al.,[17] Equation (27), and assuming the following numerical values for the stress ratio $Y_s/\sigma_x = 2$, and the radius of a die $R_0 = 1$ mm, Equation (27) yields $\lambda = 3(\frac{1}{\xi} - \xi)$. Using this form of the model, $\lambda = 3(\frac{1}{\xi} - \xi)$, the influence of the fitting parameter, b and c, of the interfacial depth parameter $\xi = b\dot{\gamma}_{app.}^{-c}$ can be parameterized. In **Figure D1**, the wavelength as a function of apparent shear rate is presented.

Supporting Information

Supporting Information is available from the Wiley Online Library or from the author.

Conflict of Interest

The authors declare no conflict of interest.

Data Availability Statement

The data that support the findings of this study are available from the corresponding author upon reasonable request.

[1] A. Leonov, A. Prokunin, *Nonlinear Phenomena in Flows of Viscoelastic Polymer Fluids*, Chapman and Hall, London **1994**.
[2] M. M. Denn, *Annu. Rev. Fluid Mech.* **2001**, *33*, 265.
[3] S. G. Hatzikiriakos, *Prog. Polym. Sci.* **2012**, *37*, 624.
[4] S. G. Hatzikiriakos, K. Migler, *Polymer Processing Instabilities. Control and Understanding*, Marcel Dekker, New York **2005**.
[5] R. Koopmans, C. F. J. den Doelder, J. Molenaar, *Polymer Melt Fracture*, CRC Press, Boca Raton, FL **2011**.
[6] S. Q. Wang, *Nonlinear Polymer Rheology: Macroscopic Phenomenology and Molecular Foundation*, John Wiley & Sons, Hoboken, NJ **2017**.
[7] S. Q. Wang, in *Polymers in Confined Environments* (Eds: K. Binder, S. Granick, K. Binder, P. G. de Gennes, E. P. Giannelis, G. S. Grest, H. Hervet, R. Krishnamoorti, L. Léger, E. Manias, E. Raphaël, S. Q. Wang), Springer, Berlin **1999**, Ch. 6.
[8] I. F. C. Naue, *Development of Improved Rheometric Tools and their Application on the Non-Newtonian Rheology of Polymeric Fluids*, Ph.D., Karlsruhe Institute of Technology (KIT), Germany **2013**.
[9] C. F. J. den Doelder, *Design and Implementation of Polymer Melt Fracture Models*, Ph.D., Eindhoven University of Technology, The Netherlands **1999**.
[10] D. Tang, F. H. Marchesini, L. Cardon, D. R. D'hooge, *Macromol. Mater. Eng.* **2020**, *305*, 2000340.
[11] M. Sentmanat, S. G. Hatzikiriakos, *Rheol. Acta* **2004**, *43*, 624.
[12] F. N. Cogswell, *J. Non-Newtonian Fluid Mech.* **1977**, *2*, 17.
[13] N. E.l Kissi, L. Léger, J. - M. Piau, A. Mezghani, *J. Non-Newtonian Fluid Mech.* **1994**, *52*, 249.
[14] N. El Kissi, J.-M. Piau, F. Toussaint, *J. Non-Newtonian Fluid Mech.* **1997**, *68*, 271.
[15] N. El Kissi, J. M. Paiu, *J. Non-Newtonian Fluid Mech.* **1990**, *37*, 55.
[16] J. M. Piau, N. El Kissi, B. Tremblay, *J. Non-Newtonian Fluid Mech.* **1990**, *34*, 145.
[17] Y. W. Inn, R. J. Fischer, M. T. Shaw, *Rheol. Acta* **1998**, *37*, 573.
[18] J.-M. Piau, N. Kissi, A. Mezghani, *J. Non-Newtonian Fluid Mech.* **1995**, *59*, 11.
[19] K. B. Migler, Y. Son, F. Qiao, K. Flynn, *J. Rheol.* **2002**, *46*, 383.
[20] C. K. Georgantopoulos, I. F. C. Naue, A. Causa, L. Garro, M. Wilhelm, *Annu. Trans. Nordic Rheol. Soc.* **2019**, *27*, 151.
[21] C. K. Georgantopoulos, M. K. Esfahani, C. Botha, I. F. C. Naue, N. Dingenouts, A. Causa, R. Kádár, M. Wilhelm, *Macromol. Mater. Eng.* **2021**, *306*, 2000801.
[22] C. K. Georgantopoulos, M. K. Esfahani, C. Botha, M. A. Pollard, I. F. C. Naue, A. Causa, R. Kádár, M. Wilhelm, *Phys. Fluids* **2021**, *33*, 093108.

**ADVANCED
SCIENCE NEWS**

www.advancedsciencenews.com

**[M] acro-
olecular
Materials and Engineering**

www.mame-journal.de

[23] T. I. Burghelea, H. J. Griess, H. Münstedt, *J. Non-Newtonian Fluid Mech.* **2010**, *165*, 1093.

[24] T. I. Burghelea, H. J. Grieß, H. Münstedt, *J. Non-Newtonian Fluid Mech.* **2012**, *173*, 87.

[25] B. Tremblay, *J. Rheol.* **1991**, *35*, 985.

[26] R. Rutgers, M. Mackley, *J. Rheol.* **2000**, *44*, 1319.

[27] C. Venet, B. Vergnes, *J. Non-Newtonian Fluid Mech.* **2000**, *93*, 117.

[28] G. Karapetsas, J. Tsamopoulos, *Phys. Fluids* **2013**, *25*, 093105.

[29] D. Pettas, G. Karapetsas, Y. Dimakopoulos, J. Tsamopoulos, *J. Non-Newtonian Fluid Mech.* **2015**, *224*, 61.

[30] S. Varchanis, D. Pettas, Y. Dimakopoulos, J. Tsamopoulos, *Phys. Rev. Lett.* **2021**, *127*, 088001.

[31] S.-Q. Wang, P. A. Drda, Y.-W. Inn, *J. Rheol.* **1996**, *40*, 875.

[32] S.-Q. Wang, P. Drda, *Macromol. Chem. Phys.* **1997**, *198*, 673.

[33] J. R. Barone, N. Plucktaveesak, S. Q. Wang, *J. Rheol.* **1998**, *42*, 813.

[34] H. Ovaici, M. R. Mackley, G. H. Mckinley, S. J. Crook, *J. Rheol.* **1998**, *42*, 125.

[35] W. Burchard, in *Branched Polymers II. Advances in Polymer Science* (Ed: J. Roovers), Vol. *143*, Springer, Berlin **1999**.

[36] J. Brandrup, E. H. Immergut, E. A. Grulke, *Polymer Handbook*, 4th ed., John Wiley & Sons, New York **1999**.

[37] F. A. Morrison, *Understanding Rheology*, Oxford University Press, New York **2001**.

[38] J. F. T. Pittman, *Proc. Inst. Mech. Eng., Part E* **2011**, *225*, 280.

[39] W. P. Cox, E. H. Merz, *J. Polym. Sci.* **1958**, *28*, 619.

[40] J. Roovers, P. M. Toporowski, *Macromolecules* **1987**, *20*, 9.

[41] R. G. Larson, *Macromolecules* **2001**, *34*, 4556.

[42] M. T. I. Juliani, L. A. Archer, S. K. Varshney, *Macromolecules* **2001**, *34*, 18.

[43] X. Chen, M. S. Rahman, H. Lee, J. Mays, T. Chang, R. Larson, *Macromolecules* **2011**, *44*, 19.

[44] J. M. Dealy, J. Wang, *Melt Rheology and its Application in the Plastic Industry*, 2nd ed., Springer, Dordrecht, The Netherlands **2013**.

[45] Y. Woo Inn, *J. Rheol.* **2013**, *57*, 393.

[46] M. Ebrahimi, M. Ansari, S. G. Hatzikiriakos, *J. Rheol.* **2015**, *59*, 885.

[47] M. Ebrahimi, M. Ansari, Y. W. Inn, S. G. Hatzikiriakos, *Phys. Fluids* **2016**, *28*, 093101.

[48] W. F. Busse, *Phys. Today* **1964**, *17*, 32.

[49] S. Filipe, A. Becker, V. C. Barroso, M. Wilhelm, *Appl. Rheol.* **2009**, *19*, 23345.

[50] H. Palza, I. F. C. Naue, M. Wilhelm, *Macromol. Rapid Commun.* **2009**, *30*, 1799.

[51] H. Palza, I. F. C. Naue, S. Filipe, A. Becker, J. Sunder, A. Göttfert, M. Wilhelm, *Kauts. Gummi Kunst.* **2010**, *63*, 456.

[52] H. Palza, B. Reznik, M. Kappes, F. Hennrich, I. F. C. Naue, M. Wilhelm, *Polymer* **2010**, *51*, 3753.